



## SOFIA Observations of 30 Doradus. II. Magnetic Fields and Large-scale Gas Kinematics

Le Ngoc Tram, Lars Bonne, Yue Hu, Enrique Lopez-Rodriguez, Jordan A Guerra, Pierre Lesaffre, Antoine Gusdorf, Thiem Hoang, Min-Young Lee, Alex Lazarian, et al.

### ► To cite this version:

Le Ngoc Tram, Lars Bonne, Yue Hu, Enrique Lopez-Rodriguez, Jordan A Guerra, et al.. SOFIA Observations of 30 Doradus. II. Magnetic Fields and Large-scale Gas Kinematics. The Astrophysical Journal, 2023, 946 (1), pp.8. 10.3847/1538-4357/acaab0 . hal-04303125

**HAL Id: hal-04303125**

**<https://hal.science/hal-04303125>**

Submitted on 23 Nov 2023

**HAL** is a multi-disciplinary open access archive for the deposit and dissemination of scientific research documents, whether they are published or not. The documents may come from teaching and research institutions in France or abroad, or from public or private research centers.

L'archive ouverte pluridisciplinaire **HAL**, est destinée au dépôt et à la diffusion de documents scientifiques de niveau recherche, publiés ou non, émanant des établissements d'enseignement et de recherche français ou étrangers, des laboratoires publics ou privés.



## SOFIA Observations of 30 Doradus. II. Magnetic Fields and Large-scale Gas Kinematics

Le Ngoc Tram<sup>1</sup>, Lars Bonne<sup>2</sup>, Yue Hu<sup>3,4</sup>, Enrique Lopez-Rodriguez<sup>5</sup>, Jordan A. Guerra<sup>6</sup>, Pierre Lesaffre<sup>7,8</sup>, Antoine Gusdorf<sup>7,8</sup>, Thiem Hoang<sup>9,10</sup>, Min-Young Lee<sup>9,10</sup>, Alex Lazarian<sup>4,11</sup>, B-G Andersson<sup>2</sup>, Simon Coudé<sup>13,14</sup>, Archana Soam<sup>15</sup>, William D. Vacca<sup>2</sup>, Hyeseung Lee<sup>9</sup>, and Michael Gordon<sup>12</sup>

<sup>1</sup> Max-Planck-Institut für Radioastronomie, Auf dem Hügel 69, D-53121, Bonn, Germany; [nle@mpifr-bonn.mpg.de](mailto:nle@mpifr-bonn.mpg.de)

<sup>2</sup> Stratospheric Observatory for Infrared Astronomy, Universities Space Research Association, NASA Ames Research Center, MS 232-11, Moffett Field, 94035 CA, USA

<sup>3</sup> Department of Physics, University of Wisconsin-Madison, Madison, WI 53706, USA

<sup>4</sup> Department of Astronomy, University of Wisconsin-Madison, Madison, WI 53706, USA

<sup>5</sup> Kavli Institute for Particle Astrophysics and Cosmology (KIPAC), Stanford University, Stanford, CA 94305, USA

<sup>6</sup> Department of Physics, Villanova University, 800 E. Lancaster Ave., Villanova, PA 19085, USA

<sup>7</sup> Laboratoire de Physique de l'École normale supérieure, ENS, Université PSL, CNRS, Sorbonne Université, Université de Paris, France

<sup>8</sup> Observatoire de Paris, PSL University, Sorbonne Université, LERMA, F-75014, Paris, France

<sup>9</sup> Korea Astronomy and Space Science Institute, Daejeon 34055, Republic of Korea

<sup>10</sup> Korea University of Science and Technology, 217 Gajeong-ro, Yuseong-gu, Daejeon, 34113, Republic of Korea

<sup>11</sup> Centro de Investigación en Astronomía, Universidad Bernardo O'Higgins, Santiago, General Gana 1760, 8370993, Chile

<sup>12</sup> Ball Aerospace, Boulder, 80301 CO, USA

<sup>13</sup> Department of Earth, Environment, and Physics, Worcester State University, Worcester, MA 01602, USA

<sup>14</sup> Center for Astrophysics | Harvard & Smithsonian, 60 Garden Street, Cambridge, MA 02138, USA

<sup>15</sup> Indian Institute of Astrophysics, II Block, Koramangala, Bengaluru 560034, India

Received 2022 May 12; revised 2022 December 6; accepted 2022 December 8; published 2023 March 21

## Abstract

The heart of the Large Magellanic Cloud, 30 Doradus, is a complex region with a clear core-halo structure. Feedback from the stellar cluster R136 has been shown to be the main source of energy creating multiple parsec-scale expanding-shells in the outer region, and carving a nebula core in the proximity of the ionization source. We present the morphology and strength of the magnetic fields ( $B$ -fields) of 30 Doradus inferred from the far-infrared polarimetric observations by SOFIA/HAWC+ at 89, 154, and 214  $\mu\text{m}$ . The  $B$ -field morphology is complex, showing bending structures around R136. In addition, we use high spectral and angular resolution [C II] observations from SOFIA/GREAT and CO(2-1) from APEX. The kinematic structure of the region correlates with the  $B$ -field morphology and shows evidence of multiple expanding-shells. Our  $B$ -field strength maps, estimated using the Davis–Chandrasekhar–Fermi method and structure-function, show variations across the cloud within a maximum of 600, 450, and 350  $\mu\text{G}$  at 89, 154, and 214  $\mu\text{m}$ , respectively. We estimated that the majority of the 30 Doradus clouds are subcritical and sub-Alfvénic. The probability distribution function of the gas density shows that the turbulence is mainly compressively driven, while the plasma beta parameter indicates supersonic turbulence. We show that the  $B$ -field is sufficient to hold the cloud structure integrity under feedback from R136. We suggest that supersonic compressive turbulence enables the local gravitational collapse and triggers a new generation of stars to form. The velocity gradient technique using [C II] and CO(2-1) is likely to confirm these suggestions.

*Unified Astronomy Thesaurus concepts:* [Interstellar dust \(836\)](#); [Interstellar dust extinction \(837\)](#); [Star formation \(1569\)](#); [Interstellar magnetic fields \(845\)](#); [Magnetic fields \(994\)](#); [Interstellar dynamics \(839\)](#); [Starlight polarization \(1571\)](#); [Large Magellanic Cloud \(903\)](#)

## 1. Introduction

In modern Astrophysics, magnetic fields ( $B$ -fields) and turbulence are believed to affect the star formation process. The  $B$ -fields support against gravitational collapse, while turbulence plays a dual role. Turbulence can against global cloud collapse, but can also produce local compression (Mac Low & Klessen 2004) with compressible and solenoidal motions acting in opposite directions (Cho & Lazarian 2003). The role of  $B$ -fields can be different depending on whether  $B$ -fields are dynamically important or subdominant (see a review in Crutcher 2012). For weak  $B$ -fields, the cloud is supercritical (the mass-to-flux ratio is greater than unity), and the  $B$ -fields are insufficient to prevent gravitational collapse. For strong  $B$ -fields, the fields are strong

enough to counteract the collapse. In this case, other mechanisms must be invoked for star formation to occur in the subcritical cloud (the mass-to-flux ratio is lower than unity). There are two candidates for such mechanisms: (1) ambipolar diffusion (e.g., Mestel 1966) can increase the mass faster than the  $B$ -field strength, enhancing the gravitational counterpart, and (2) fast turbulent reconnection (Lazarian & Vishniac 1999) removes the magnetic flux, weakening the magnetic support. These two mechanisms are able to increase the mass-to-flux ratio, which can lead clouds to collapse and possibly to coexist (Lazarian 2014).

The fast turbulent reconnection induces a turbulence cascade perpendicular to the ambient  $B$ -fields. As a result, turbulent eddies can freely mix the  $B$ -fields parallel to the rotation axes, where the velocity gradients (VGs) are perpendicular to the local direction of  $B$ -fields. This is the basis of the velocity gradient technique (VGT; González-Casanova & Lazarian 2017) to study  $B$ -fields in diffuse gas (Yuen & Lazarian 2017a; Hu et al. 2018, 2019a; Lazarian & Yuen 2018; Lazarian et al. 2018), in



Original content from this work may be used under the terms of the [Creative Commons Attribution 4.0 licence](#). Any further distribution of this work must maintain attribution to the author(s) and the title of the work, journal citation and DOI.

molecular clouds (Hu et al. 2019b, 2021; Hu et al. 2022; Tang et al. 2019; Alina et al. 2022), and in the atomic–molecular transition (Skalidis et al. 2022). Nevertheless, self-gravity is able to break that relationship. The gravitational forces pull the gas in the direction along the  $B$ -fields, so the VGs are dominated by the infall acceleration. In this case, the VGs are parallel to the ambient  $B$ -fields. The misalignment between VGT and  $B$ -fields becomes a proxy for the gravitational collapse (Yuen & Lazarian 2017b; Lazarian & Yuen 2018; Tang et al. 2019; Hu et al. 2021). Therefore, VGT is a promising tool to probe the  $B$ -field morphology and the local gravitational collapse.

The  $B$ -fields, turbulence, and stellar feedback shape the cloud and regulate the star formation processes. The simulations with uniform  $B$ -fields from Henney et al. (2009), Mackey & Lim (2011) showed that the  $B$ -fields have a significant contribution in shaping the cloud. This result depends on the orientation between the initial  $B$ -fields and the radiation from the source. Specifically, these authors found that clouds are flatter (broad head) if the  $B$ -fields are parallel to the radiation direction, while the cloud becomes a more elongated structure (tail-like structure) if the  $B$ -fields are perpendicular to the radiation direction. These features appear to be confirmed from observations, e.g., IC 1396 (Soam et al. 2018a), M16 (Pattle et al. 2018), Ophiuchus-A (Santos et al. 2019). The simulations of the feedback in a turbulent magnetized cloud by Arthur et al. (2011) showed that the  $B$ -fields tend to be amplified and slow down the formation of stars.

The morphology of the  $B$ -fields is affected by gravity (resulting in a well-known hour-glass shape; Ewertowski & Basu 2013), and regulated by the supersonic gas motion as proposed by Inoue & Fukui (2013). The latter seems to be frequently observed, e.g., deformation of  $B$ -field geometry in M16 (Pattle et al. 2018), Orion-A (Tahani et al. 2019), Musca filament (Bonne et al. 2020a, 2020b), and BHR 71 bipolar outflow system (Kandori et al. 2020). Using simulations, Abe et al. (2021) demonstrated that a shock with a velocity of  $\sim 7 \text{ km s}^{-1}$  is able to wrap the  $B$ -fields.

Even though  $B$ -fields may affect the star formation processes, the direct measurement of  $B$ -fields is difficult. Alternatively, the  $B$ -fields are inferred using several data analysis methods. One of the methods consists in using dust polarization (see, e.g., Lazarian 2007; and Andersson et al. 2015 for reviews). The basic idea of this technique relies on the fact that irregular dust grains tend to align with their shortest axis parallel to the local  $B$ -fields due to various physical effects (see, e.g., Hoang et al. 2022a for details) so that their thermal emission is polarized with the polarization orientation perpendicular to the  $B$ -fields (see Tram & Hoang 2022). The measured position angle of thermal dust polarization is then perpendicular to the local  $B$ -fields in the plane of the sky. Hence, the polarimetric data allows us to map the  $B$ -field geometry by rotating the polarization angles by  $90^\circ$ . The polarized thermal dust emission is feasible at long wavelengths, i.e., far-infrared (FIR) to submillimeter. The strength of the  $B$ -fields on the plane of the sky ( $B_{\text{POS}}$ ) can be estimated using the Davis–Chandrasekhar–Fermi (DCF; Davis 1951; Chandrasekhar & Fermi 1953) method. This method is commonly used, although some modifications need to be taken into account as a function of the object to be analyzed (Liu et al. 2022). Another approach (namely the differential measure approach, or DMA) is recently proposed by Lazarian et al. (2020, 2022), which is suggested to be able to measure the  $B$ -field strength more precisely.

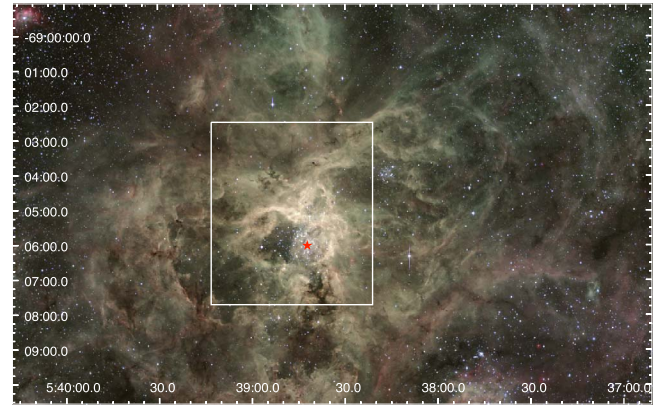


**Figure 1.** Public composite image of 30 Dor observed by La Silla 2.2 m telescope with  $H\alpha$ -658.827 nm (red), a combination of V-539.562 nm and [O III]-502.393 nm (green), and B-451.100 nm (blue). This image shows a complex structure of the region with multiple large expanding-shells produced by the hot cluster-wind from R136 (indicated by a red star), and a slow expanding-shell from the supernova remnant 30DorB (lower right). The white box shows the region covered by SOFIA/HAWC+ that we analyze in this work.

Our target is the star formation region 30 Doradus (hereafter 30 Dor) in the Large Magellanic Cloud (LMC). With a distance of  $\sim 50$  kpc away from Earth (Schaefer 2008), it is close enough to obtain parsec-scale resolutions to study the impact of the feedback and turbulence on the surrounding molecular cloud. 30 Dor hosts a massive star cluster, R136, which is associated to the H II giant expanding-shells (Kennicutt 1984; Chu & Kennicutt 1994; Brandl 2005; Townsley et al. 2006; Lopez et al. 2011), and a nearby supernova remnant (Townsley et al. 2006). Figure 1<sup>16</sup> shows a composite image of the 30 Dor region with an overlay of the field of view covered in our study. This complex system is embedded by multiple H I giant-shells (Kim et al. 1999). A combination of stellar winds and supernovae (Chu & Kennicutt 1994) or only the cluster-wind (not the stellar wind of individual stars) from R136 (Melnick et al. 2021) are demonstrated to be the main sources to create these giant H II expanding-structures. The authors also clearly unveiled two structures in 30 Dor. For the nebula’s core (within a distance of 25 pc proximity to R136), surprisingly, the thermal gas pressure is lower than that of the stellar radiation (see Figure 18 in Pellegrini et al. 2011), and the mass is lower than the virial mass (Melnick et al. 2021). Hence, the important questions remaining are as follows: How can this structure survive? And how can stars form? (The locations of protostar candidates are shown in, e.g., Lee et al. 2019; Indebetouw et al. 2009). Here, we focus on the closest region to R136, which is indicated by the white box in Figure 1. For the sake of simplicity, we refer to this region as 30 Dor in this work.

Our goals are to

1. map the morphology and strength of the  $B$ -fields in 30 Dor using FIR polarimetric observations with SOFIA/HAWC+ as introduced in Tram et al. (2021c; hereafter Paper I);
2. examine the gas kinematic in 30 Dor by making use of [C II] and CO(2-1) data acquired by SOFIA/GREAT and APEX (see Okada et al. 2019);

<sup>16</sup> Public data at <https://archive.eso.org/cms/eso-data/data-packages/30-doradus.html>.

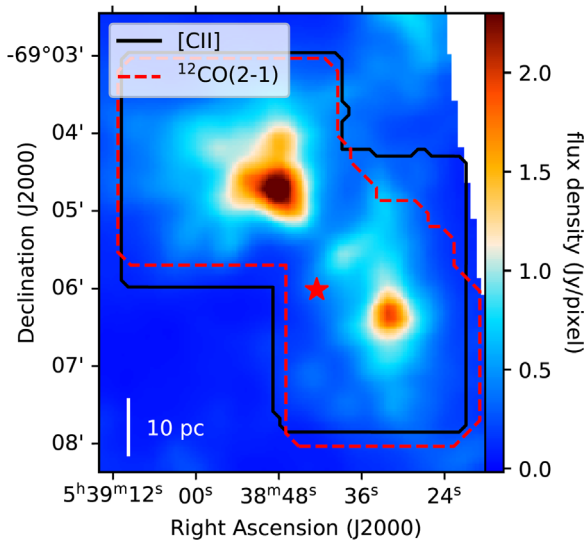


**Figure 2.** HAWC+ dust continuum flux density map at  $214\ \mu\text{m}$ . The black full line indicates the region that is covered by the [C II] observations, and the red dashed line outlines the region covered by the  $^{12}\text{CO}(2-1)$  observations (Okada et al. 2019). The red star indicates the location of R136.

3. make use of the VGT to probe the local gravitational collapse in 30 Dor;
4. quantify the effect of  $B$ -fields on supporting the cloud integrity; and
5. perform an energy budget to quantify the effect of gravity,  $B$ -fields, and turbulence on the star-forming processes of 30 Dor.

This paper is structured as follows. We analyze the gas kinematics in Section 2. The analysis of the  $B$ -field orientations and strengths are shown in Section 3. Our discussions are presented in Section 4. The conclusions are presented in Section 5.

## 2. Large-scale Kinematics in 30 Doradus

To analyze the parsec-scale kinematics of 30 Dor at the location of the SOFIA/HAWC+ observations, we make use of the spectral lines presented in Okada et al. (2019) that were observed with SOFIA (Young et al. 2012) and the APEX telescope (Güsten et al. 2006). For details on the data reduction, we refer to Okada et al. (2019). The SOFIA observations of the [C II] line have a spatial resolution of  $16''$ , and the APEX  $^{12}\text{CO}(2-1)$  observations have a spatial resolution of  $30''$ . The region of the HAWC+ map and of the [C II] and  $^{12}\text{CO}(2-1)$  is presented in Figure 2. Both lines cover a similar area of 30 Dor where the dust polarization is detected.

### 2.1. The Integrated Intensity Maps

In Figure 3, the integrated intensity maps of [C II] and  $^{12}\text{CO}(2-1)$  are compared with the dust continuum maps from HAWC+ at  $214\ \mu\text{m}$ . This figure shows that the [C II] peak intensities are closely correlated with the dust continuum peak and that it also traces the extended emission. We find that  $^{12}\text{CO}(2-1)$  is more sensitive to the gas located in the high column density regions, which can be expected for this lower metallicity region. As a result, the [C II] emission will be more sensitive to the kinematics of the ambient gas, whereas CO is more sensitive to the dense clumps in the cloud.

### 2.2. The Velocity Structure of 30 Doradus

In Okada et al. (2019) and Figure 3, several [C II] and CO spectra of 30 Dor are presented. These observations show that most of the emission is found between  $220$  and  $280\ \text{km s}^{-1}$ . In this velocity range, multiple velocity components and high-velocity wings are observed. In Figure 3, the wings are most clear in spectra (1)–(4) and specifically in the velocity range between  $220$  and  $240\ \text{km s}^{-1}$  and between  $255$  and  $280\ \text{km s}^{-1}$ . Such wing-like structures were recently also found in spectrally resolved [C II] observations toward galactic H II regions (e.g., Schneider et al. 2018, 2020; Tiwari et al. 2021; Bonne et al. 2022a). The 30 Dor region has a complex dynamical structure. This is illustrated in more detail for [C II] and  $^{12}\text{CO}(2-1)$  in Figures 4 and 15 (in Appendix A). Despite the complexity of the kinematics, Figure 4 shows that both lines have a broadly similar velocity structure on large scales. Inspecting the velocity structure in Figure 4, it can be noted, in particular with [C II], that the blueshifted and redshifted gas appear to create intersecting axes toward the middle of the SOFIA map. This intersection is shown in Figure 4 by the northeast-to-southwest axis for blueshifted velocities and the east-to-west axis for redshifted velocities. This intersecting structure formed by the blue and red axis is also observed in the channel maps of the region that are presented in Figure 15 of Appendix A. The channel maps also confirm that the southern part of the maps consists of two subregions, which are discontinuous in velocity. This is consistent with the SOFIA/HAWC+ integrated maps, which show that this western region contains two clumps. Furthermore, these two subregions have a noticeably different  $B$ -field structure in Figure 9. In the northern region of the map, it is also observed that there is a noteworthy change in  $B$ -field orientation at the transition from blueshifted to redshifted gas, which confirms that the  $B$ -field morphology is directly related to the large-scale kinematics of the 30 Dor region; see Figure 4.

From the data cubes, the moment maps can be calculated. However, before presenting these moment maps, it has to be noted that there are limitations to the moment maps due to the inherent complexity (i.e., multiple components and high-velocity wings) in the spectra. The resulting moment maps are presented in Figure 5. The first-moment map (or the velocity field) has an organized gradient that looks similar in [C II] and  $^{12}\text{CO}(2-1)$  and fits with the velocity field obtained at smaller scales with Atacama Large Millimeter/submillimeter Array observations (Indebetouw et al. 2013). Even though both lines show a similar morphology, it is found that the [C II] velocity field covers a significantly larger velocity range. The CO kinematics thus tend to follow the [C II] kinematics, but less drastically.

Both lines are expected to trace different regions in the cloud because of the critical density<sup>17</sup> and the fact that far-UV radiation propagates farther into the cloud in low-metallicity regions. From the second-moment maps, presented in Figure 5, it is observed that the line width significantly depends on the observed line. For this, it has to be taken into account that there are indications of multiple components, also reported in Melnick et al. (2021), which are particularly clear in [C II].

<sup>17</sup> The critical density is defined by the balance between collisional deexcitation and spontaneous decay. The collisional rate and Einstein coefficients are adopted from <https://home.strw.leidenuniv.nl/~moldata/>. For [C II] and CO(2-1), this gives values of the order of  $10^3$  and  $10^4\ \text{cm}^{-3}$ , respectively.

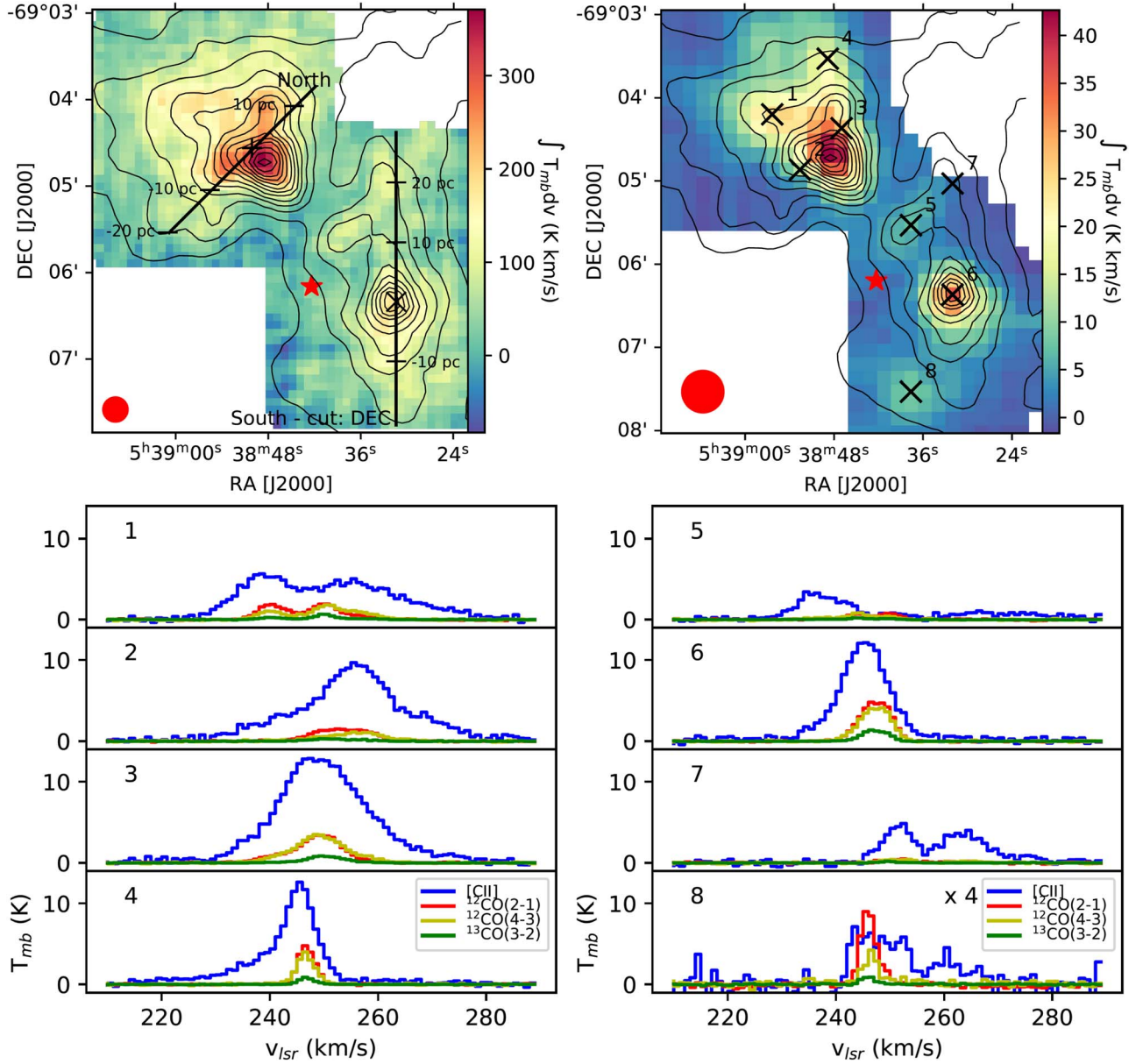


**Figure 3.** Left: [C II] integrated intensity map of 30 Dor. The black contours show the HAWC+ dust continuum emission at  $214\ \mu\text{m}$  starting at  $0.1\ \text{Jy pixel}^{-1}$  with increments of  $0.1\ \text{Jy pixel}^{-1}$ . The two lines indicate the spatial axes that were used to construct the position–velocity (PV) diagrams presented in Figure 6. The crosses indicate the center, i.e., 0 pc, of the PV diagrams, and the horizontal locations indicate the physical distance along the axis at the location of 30 Dor. The red star indicates the location of R136. Right: the integrated intensity map of  $^{12}\text{CO}(2-1)$ , overlaid with the same HAWC+ contours shown on the left. The crosses indicate the spatial locations of the spectra shown below. Bottom: the extracted [C II],  $^{12}\text{CO}(2-1)$ ,  $^{12}\text{CO}(4-3)$ , and  $^{13}\text{CO}(3-2)$  spectra at the indicated locations over the 30 Dor region, displaying multiple components and several wings in [C II].

For example, two velocity components are prominent in the most northeastern part of the map (see Figure 3), which is translated in a large second moment in that region. From the maps, it is also observed that the northern region has a higher second moment than that of the southern region, which could be related to the smaller velocity range covered by the velocity field in that region. Both lines do show a common behavior for the second moment over the map. Specifically, they show a reduction in the line width toward the densest gas of the northern and southern regions.

### 2.3. Position–Velocity Diagrams of 30 Doradus

The *B*-field observations of 30 Dor, presented in Figure 9, unveil a relatively organized structure in most regions of the

cloud. As a result, it defines the main direction for both the northern clump and the southern regions of the map. This direction of the magnetic field in both regions will be used to study the [C II] kinematics of 30 Dor using position–velocity (PV) diagrams. These two directions, which are aligned with the mean field lines, are presented in Figure 3. Additionally, cuts through 4 regions in the RA direction were made for PV diagrams of [C II]. The location of these cuts is presented in Figure 5. All the resulting PV diagrams are presented in Figure 6.

These PV diagrams confirm that there are several organized VGs in the region. These gradients cover a velocity interval of  $5\text{--}15\ \text{km s}^{-1}$  in most PV diagrams and come in the form of curves/half-elliptical features that have been associated with

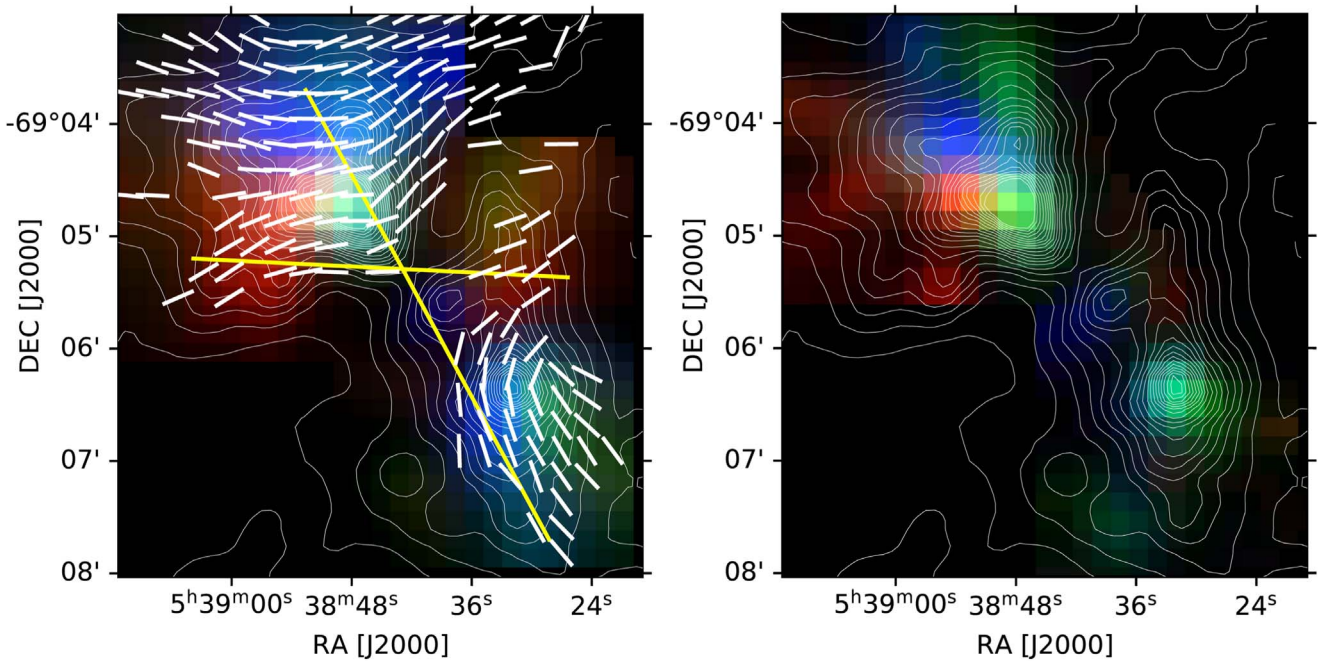


**Figure 4.** Left: RGB image of 30 Dor for [C II] with blue, 235–245 km s<sup>−1</sup>; green, 245–255 km s<sup>−1</sup>; and red, 255–270 km s<sup>−1</sup>. The contours indicate the HAWC+ 214 μm dust continuum emission starting at 0.1 Jy pixel<sup>−1</sup> with increments of 0.1 Jy pixel<sup>−1</sup>. The yellow cross is added to guide the eye at the axes of what appears to be dominantly blueshifted and redshifted gas. The white segments indicate the magnetic field morphology on the RGB image. Right: the same for <sup>12</sup>CO(2-1).

expanding-shells (Pabst et al. 2019, 2020; Luisi et al. 2021; Tiwari et al. 2021; Beuther et al. 2022; Bonne et al. 2022a). Based on the presence of these curved features, we identify 4 expanding-shell candidates over the full map using the PV diagrams. The curved velocity structures associated with the candidate expanding-shells are indicated in Figure 6. With the channel maps in Figure 15, we confirm that these candidates have a spatially curved/ring-like morphology as expected for expanding-shell features. We name these candidate expanding-shells: north, east, west, and south after their locations on the map. The location and velocity range of these expanding-shell candidates are presented in Table 1. The location of these shell candidates is also indicated over their velocity range in Figure 15. Two expanding-shell candidates are found in the range of 230–250 km s<sup>−1</sup>, and two are found in the range of 250–265 km s<sup>−1</sup>. As some of these shells appear to be only partly covered, larger maps will be required to study their full extent, better characterize their properties, and investigate whether some of the identified shells have the same expansion origin or not. This will also help to study, in combination with data at different wavelengths, whether radiation or stellar winds drive these expanding-shell motions. As the expanding-shells are directly identified by the two blue and red regions in the composite (RGB) image in Figure 4, this shows that the *B*-field curvature is associated with these expanding [C II] shell candidates. The highest-density region in the northern region is located at the intersection of two expanding-shells. It might be possible that this region is formed by the collision of the two expanding features. This could result in additional magnetic field bending through oblique shocks (e.g., Inoue & Fukui 2013; Bonne et al. 2020b). However, in the complex dynamical structure, and with the limited spectral [C II] resolution, it is not easy to establish indications of such *B*-field bending with confidence. Additionally, the increasing role

of gravity might also alter the *B*-field morphology in this high-density region.

#### 2.4. Velocity Gradient Technique

In this section, we computed the VGs of both [C II] and CO(2-1) from their channel maps adopted from Hu et al. (2021), which is referred to as VChGs (Lazarian & Yuen 2018). Here we recall the principle of this method. The methodology follows these steps: (1) the initial position–position–velocity datacube was preprocessed using principle component analysis by splitting a very large number of velocity channels along the line of sight (LOS) as long as the thin channel map<sup>18</sup> criteria is satisfied (Lazarian & Pogosyan 2000); (2) the product was convoluted with a  $3 \times 3$  Sobel Kernel to create a raw gradient map (pixels are blanked out if their intensity is less than 3 times root-mean-square level); (3) the gradient angle at each pixel was statistically computed from an adaptive subblock<sup>19</sup> average method (Yuen & Lazarian 2017a), in which all single gradient orientation within a rectangle subblock in the raw gradient map was taken into account; (4) the pseudo-Stokes Q and U of the gradient were created (Lu et al. 2020), which allows computing the VG morphology. As the principle of VGT, the *B*-fields are inferred from this technique by rotating the VG orientation by 90° (González-Casanova & Lazarian 2017). However, please note that the zero-angle of the VGs is defined along the east–west direction, which is an offset angle of the polarization angle defined by the SOFIA/HAWC+. Therefore, the VG orientation naturally infers the *B*-fields in the frame of the SOFIA/HAWC+ thermal dust polarization.

<sup>18</sup> A thin velocity channel does have information of the density and velocity fluctuation, but it is more sensitive to the velocity as the channel gets thinner so that the channel map will be used to compute the VG.

<sup>19</sup> The size of the subblock was chosen such that the histogram of the gradient orientation within this block follows a Gaussian distribution.

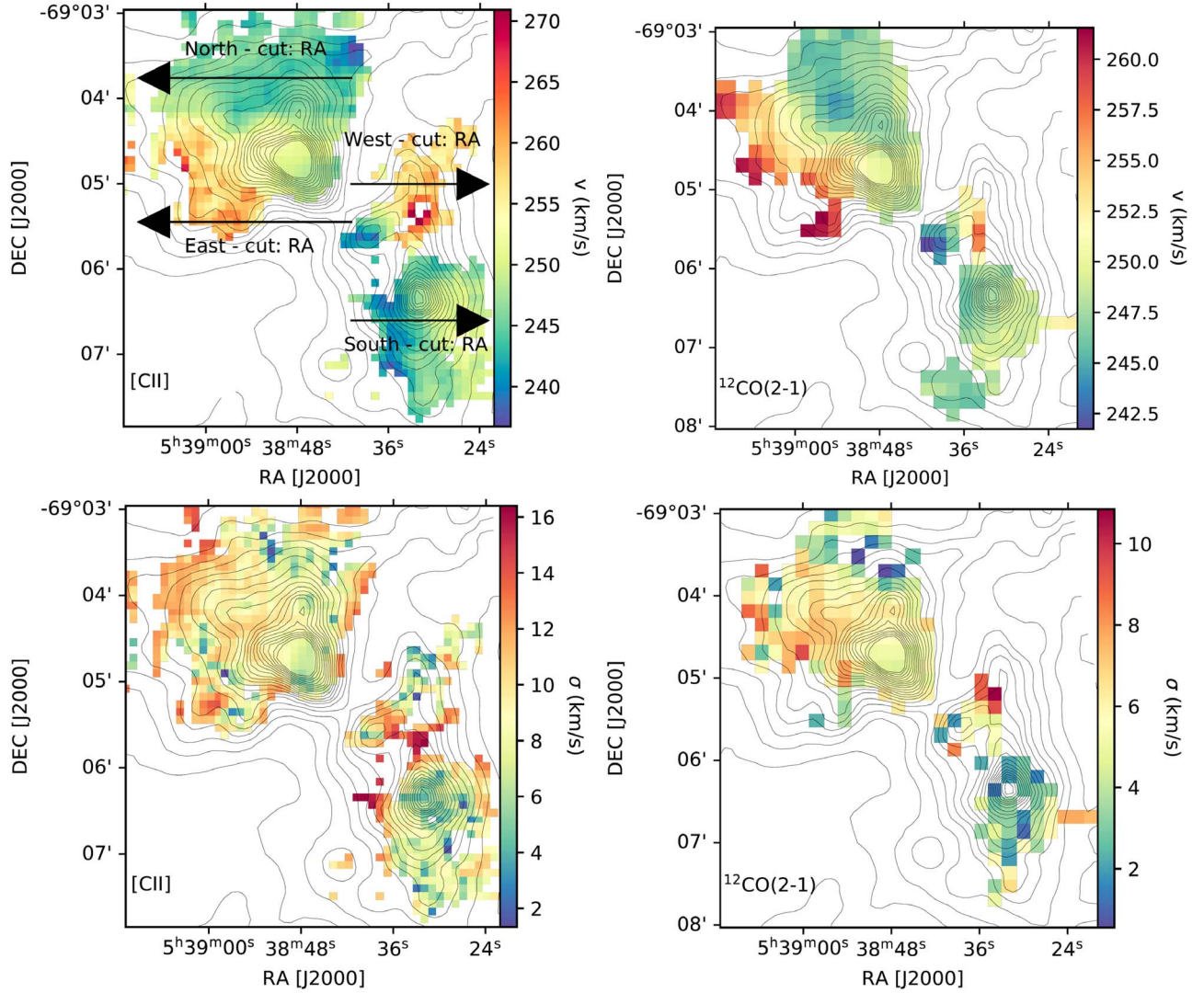


**Figure 5.** Upper left: first-moment map obtained with the [C II] line. The black contours indicate the HAWC+ emission at  $214\ \mu\text{m}$  starting at  $0.1\ \text{Jy pixel}^{-1}$  with increments of  $0.1\ \text{Jy pixel}^{-1}$ . The black arrows indicate the regions, with their name, for the position–velocity (PV) diagrams presented in Figure 6. The arrows indicate the increasing distance ( $d$ ) in the PV diagrams. Lower left: the second-moment map of [C II]. Right: the same for  $^{12}\text{CO}(2-1)$ .

Figure 7 shows the  $B$ -fields inferred by the VGTs (red vectors) from both [C II] (left panel) and CO(2-1) (right panel). To measure the correlation between  $B$ -fields inferred from VGTs and SOFIA/HAWC+ (black vectors), we computed the local alignment measurement (AM) as (González-Casanova & Lazarian 2017)

$$\text{AM} = 2 \left( \cos^2 \theta_r - \frac{1}{2} \right), \quad (1)$$

with  $\theta_r = |\theta_{\text{VG}} - \theta_{\text{HAWC+}}|$  the angle differences between VGT and HAWC+. These two vectors are parallel when  $\text{AM} = 1$ , while they become perpendicular once  $\text{AM} = -1$ .  $\text{AM} < 0$  indicates where these two vectors are misaligned (i.e., VGs are parallel to  $B$ -field lines). One can see that the VGT agrees well with the dust polarization in the south (i.e., VGs are perpendicular to  $B$ -field lines), but only fairly in the north. The VGT computed by [C II] shows that the misalignment occurs mostly at the edge of the regions where the gas density is not peaked (see Paper I). The VGT from CO(2-1) further shows that the misalignment occurs at the denser regions. The

reason is that [C II] traces for more diffuse gas than CO so that it is less affected by gravity.

### 3. Magnetic Fields in 30 Doradus

To map the  $B$ -fields of 30 Dor, we make use of the SOFIA/HAWC+ polarimetric data at  $89$ ,  $154$ , and  $214\ \mu\text{m}$  observed under the Strategic Director’s Discretionary Time (S-DDT) program (PI: Yorke, H., ID: 76\_0001) during the SOFIA New Zealand deployment in 2018 July. The reduction of data was introduced in Gordon et al. (2018).

#### 3.1. Magnetic Field Morphology

Assuming grains are perfectly aligned with the  $B$ -fields,<sup>20</sup> Figure 9 shows the geometry of the fields for all three bands (top to bottom), which is inferred from the polarization orientations. The background color is the original total intensity (Stokes I). One can see that there are two main regions in 30 Dor, these are the north and south regions relative to the

<sup>20</sup> We validate this assumption in the upcoming work (L. N. Tram et al. 2023, in preparation).

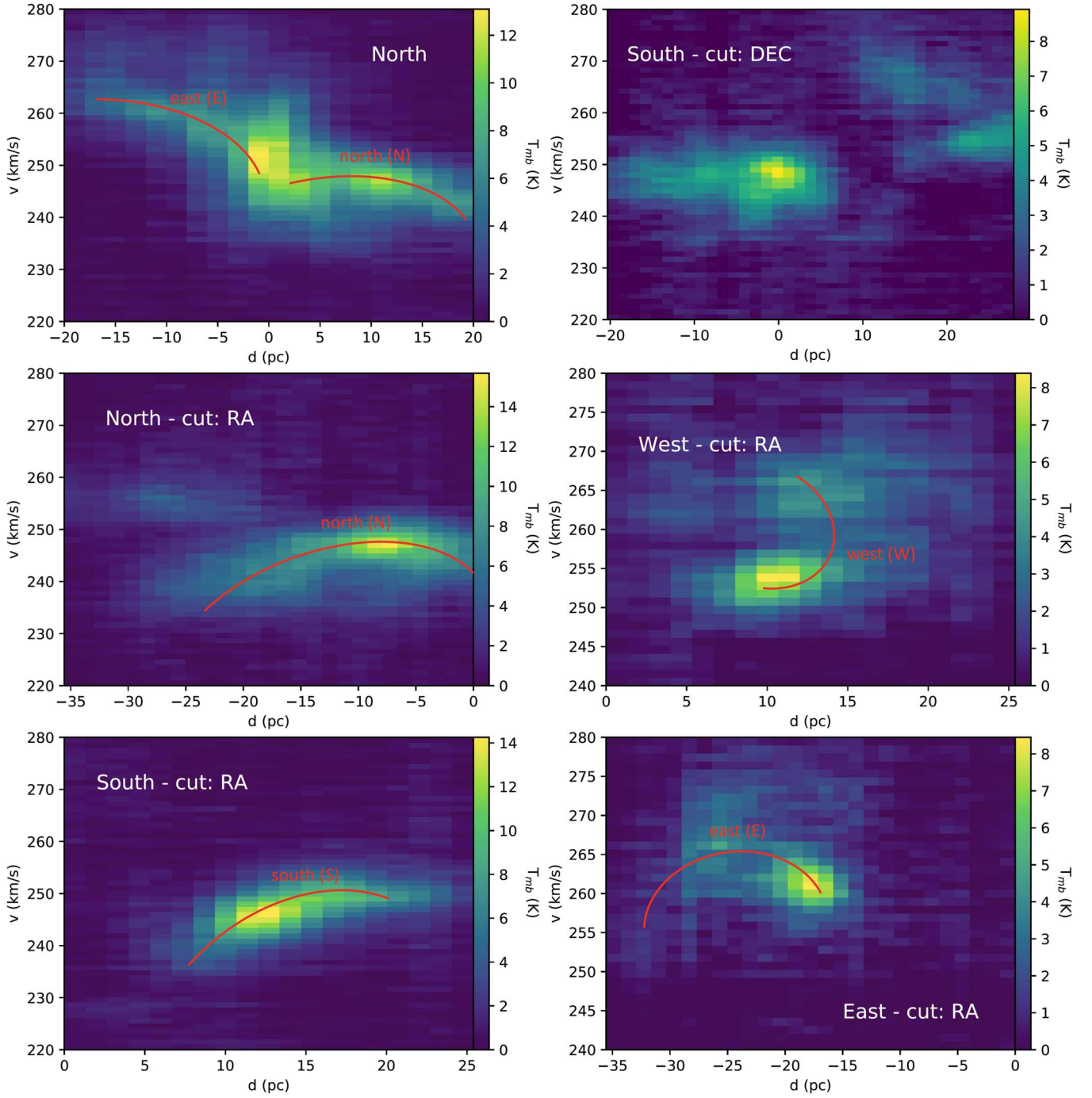


**Figure 6.** [C II] position–velocity (PV) diagrams, with a spatial resolution of  $\sim 4$  pc and a spectral resolution of  $0.5 \text{ km s}^{-1}$ , over multiple regions of the 30 Dor cloud at the locations indicated by the name in white. The cuts used to produce the PV diagrams in the top row are indicated in Figure 3, and the cuts used to produce the PV diagrams in the two bottom rows are indicated in Figure 5. All cuts show large gradients, often with a curve like nature, over  $5\text{--}15 \text{ km s}^{-1}$ , which could be associated with the presence of multiple expanding-shells in this cloud. These candidate expanding-shells, with their name, are indicated in red.

massive star cluster R136, whose center is located by the red star. The  $B$ -fields are complex but highly ordered, and show a curved feature around the peak intensity (or the peak gas density) in both the north and the south regions. The field lines are curved toward the central cluster. In addition, the field structure at the east side of the peaked intensity in the north region looks like an hourglass. These behaviors are observed similarly in all three bands. The discrepancy among the three panels shown in Figure 9 is mainly due to the fact that the

shorter wavelength has higher spatial resolution than those of the longer ones.

### 3.2. Magnetic Field Strength

The distortion of the  $B$ -field morphology could result from the local conditions. For example, this could possibly be explained by the compression of the  $B$ -fields by turbulence, shock (Inoue & Fukui 2013), or gravitational contraction

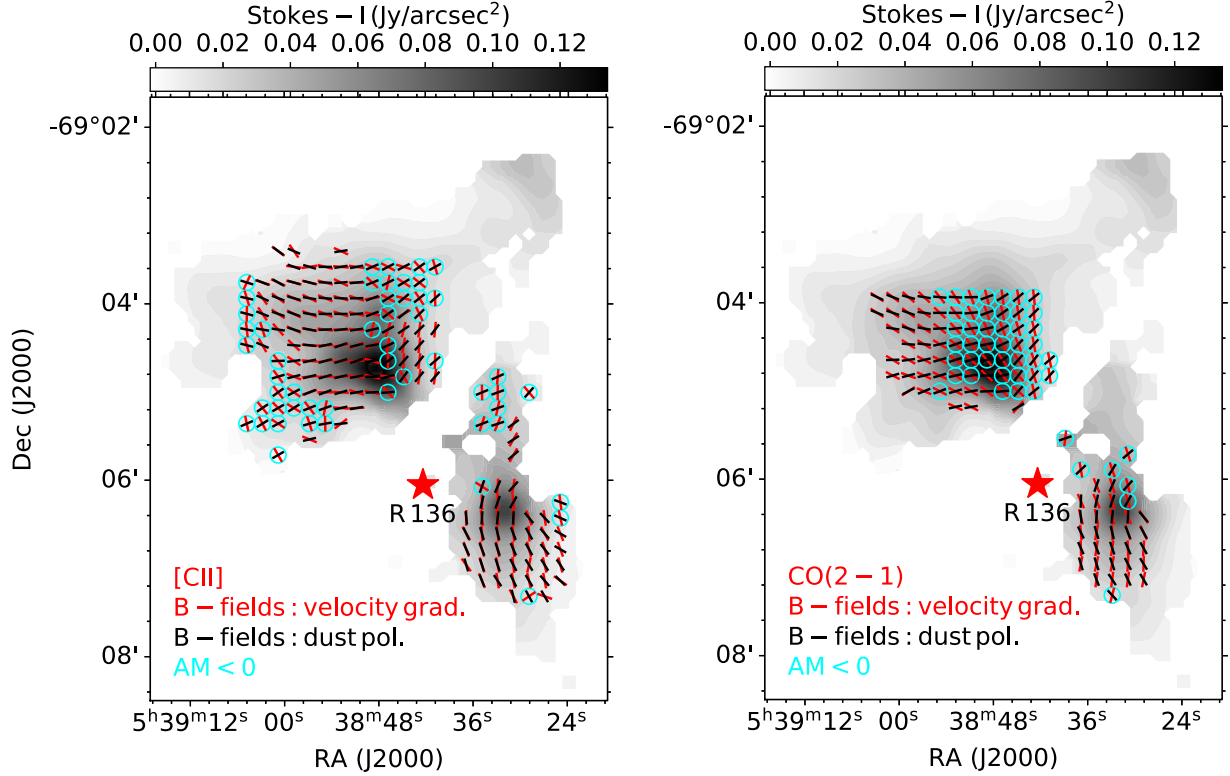


**Figure 7.** Comparison of  $B$ -fields inferred from the VGTs (red) and from the thermal dust polarization (black). The VGs estimated from [C II] are shown on the left, and from CO(2-1) on the right. The cyan circles indicate where these inferred magnetic fields are misaligned (i.e., the velocity gradient is parallel to the field lines). The background is the total dust intensity at  $214 \mu\text{m}$ .

**Table 1**

The Location and Velocity Range for the Identified Expanding-shell Features in the 30 Dor Region

Expanding-shell Candidates			
Location	$\alpha_{J2000}$	$\delta_{J2000}$	Velocities ( $\text{km s}^{-1}$ )
North (N)	05:38:55	−69:04:00	230–250
East (E)	05:38:55	−69:05:30	250–265
West (W)	05:38:32	−69:05:00	250–265
South (S)	05:38:32	−69:06:30	235–250

(Ewertowski & Basu 2013). To address which is a likely cause of this interesting situation and the local effect of the  $B$ -fields, we thus estimate the map of the  $B$ -field strength.

We determine the spatial distribution of the  $B$ -field strength in 30 Dor according to the strategy developed by Guerra et al. (2021):

1. A map of the strength of the  $B_{\text{POS}}$  can be determined using the DCF (Davis 1951; Chandrasekhar & Fermi 1953), based on the equipartition of the turbulent magnetic energy and the turbulent kinematic energy approximation:

$$B_{\text{POS}} \simeq \sqrt{4\pi\rho} \frac{\delta V_t}{\delta\phi}, \quad (2)$$

where  $\delta V_t$  is a map of the velocity dispersion of the gas,  $\rho$  is the map of the gas density, and  $\delta\phi$  is a map of the angle dispersion of the polarization orientation. Following a modification in Houde et al. (2009), the angle dispersion

is replaced by the angular dispersion (or structure-function) proportional to the ratio of large-to-small-scale magnetic energies as  $\delta\phi \simeq [\langle B_l^2 \rangle / \langle B_0^2 \rangle]^{1/2}$ . This improvement is able to avoid the spatial change in the  $B$ -field morphology with  $\langle B_l^2 \rangle / \langle B_0^2 \rangle$ .

2. The structure-function dispersion analysis (Houde et al. 2009) was applied to every map of  $B$ -field angles ( $\phi$ ) in a pixel-by-pixel fashion. This means, for a given pixel  $i$ , a circular kernel of radius  $w$ -pixel is defined around it. All the pixels inside this kernel are then used to calculate the dispersion function  $1 - \langle \cos[\Delta\phi(\ell)] \rangle$  for pixel  $i$ . This dispersion function can be described by the two-scale model:

$$1 - \langle \cos[\Delta\phi(\ell)] \rangle = \frac{1 - e^{-\ell^2/2(\delta^2 + 2W^2)}}{1 + \mathcal{N}\left[\frac{\langle B_l^2 \rangle}{\langle B_0^2 \rangle}\right]^{-1}} + a_2 \ell^2, \quad (3)$$

where  $\Delta\phi(\ell)$  is the difference between a pair of  $\phi$  separated by the distance  $\ell$ . The first term in Equation (3) describes the small-scale, turbulent  $B$  contribution to the dispersion. In this term,  $\delta$  is the turbulence correlation length,  $\mathcal{N}(=\Delta(\delta^2 + 2W^2)/\sqrt{2\pi\delta^3})$  is the number of turbulent cells along the LOS, and  $W$  is the beam's radius (e.g., the  $\sigma$  value) of the polarimetric observations.  $\Delta'$ —the cloud's effective depth—is used as a proxy for the depth along the LOS (see Houde et al. 2009 for definition). The second term in Equation (3) quantifies the contribution from the large-scale, ordered magnetic field to the dispersion function.

3. The dispersion function in every pixel is fitted with Equation (3) using a Markov Chain Monte Carlo

**Table 2**

Values of Turbulence Correlation Length ( $\delta$ ), Correlated Beam Size ( $\sqrt{2}W$ ), and Optimal Kernel Size ( $w_{\text{opt}}$ ) for the Map-making Procedure (Top)

30 Dor	$\lambda$ ( $\mu\text{m}$ )	$\delta$ ( $''$ )	$\sqrt{2}W$ ( $''$ )	$w_{\text{opt}}$ ( $''$ )
	89	16.00	4.68	17.55
	154	21.56	8.17	30.51
	214	23.68	10.93	40.95
North	$\lambda$ ( $\mu\text{m}$ )	$\Delta'$ (arcmin)	$\Delta'$ (pc)	
	89	0.55	7.84	
	154	0.74	10.53	
	214	0.76	10.82	
South	$\lambda$ ( $\mu\text{m}$ )	$\Delta'$ (arcmin)	$\Delta'$ (pc)	
	89	0.33	4.70	
	154	0.40	5.70	
	214	0.38	5.41	

**Note.** Cloud’s effective thickness ( $\Delta'$ ) for the north (middle) and south (bottom) regions of 30 Dor. These values were calculated as the half-width half-max of the 1D autocorrelation of the polarized flux at each wavelength. Linear depths are calculated from angular depths assuming a distance of 49 kpc.

(MCMC) solver. This fitting process can determine values of  $\langle B_t^2 \rangle / \langle B_0^2 \rangle$ ,  $a_2$ , and  $\delta$  in every pixel. The map of  $\langle B_t^2 \rangle / \langle B_0^2 \rangle$  is required to estimate the  $B_{\text{POS}}$  strength.

- Before combining all three maps through Equation (2), they must have the same angular resolution. In order to do that, the lowest angular resolution (target resolution;  $\sigma_T$ ) among  $\delta V$ ,  $\rho$ , and  $\langle B_t^2 \rangle / \langle B_0^2 \rangle$  is chosen, and the other maps are smoothed using a Gaussian kernel with width  $\sigma^2 \rightarrow \sigma_T^2 - \sigma^2$ .

The choice of kernel size,  $w$ , is important for the fitted values of  $\langle B_t^2 \rangle / \langle B_0^2 \rangle$ ,  $a_2$ ,  $\delta$  (if fitted), and therefore the  $B_{\text{POS}}$  maps. According to Guerra et al. (2021), the kernel size needs to be large enough to result in statistically significant dispersion functions but small enough for any resulting map to have meaningful angular resolution and avoid smoothing them over large areas. The optimal kernel size,  $w_{\text{opt}}$ , can be found by monitoring the distribution of  $\rho^{21}$  values—between the constructed dispersion function and its fit in every pixel. We performed tests using the 214  $\mu\text{m}$  map and values of  $w = 7, 9, 11$  pixels, and found that  $w = 9$  pixels produced the largest fraction of pixels with  $\rho \sim 1$ . Table 2 shows the values of  $w_{\text{opt}}$ , global  $\delta$ , and correlated beam size ( $\sqrt{2}W$ ) for all three bands. From these values, it is clear that the 9 pixel-radius circular kernel contains 7.5 correlated beams and 2–3 turbulence correlation lengths.

Using kernels with  $w > w_{\text{opt}}$  will not result in better-determined fitting parameters since the addition of more pairs of vectors will not modify the small-scale portion of the dispersion function. Instead, it will result in the contribution of scales larger than those described by the term  $\propto \ell^2$ , which are not described by the model in Equation (3).

In order to evaluate Equation (2), we used the  $N(\text{H}_2)$  map from Paper I, and for  $\delta V$  we used the second-moment map of either CO or [C II] (Figure 5). To transform column density to mass density, the cloud’s depth must be used. In this work, we used the  $\Delta'$  defined above, which is calculated as the width of the autocorrelation function of the polarized intensity. However, taking into consideration that the 30 Dor complex is distinctly separated into two clumps, assuming one single value for  $\Delta'$  can result in less accurate values of  $B_{\text{POS}}$ . Therefore, we created a map of  $\Delta'$  that consists of two areas (north and south) each with a constant, different value. These values are displayed in Table 2. On the other hand, the second moment ( $\delta V$ ), calculated from CO and [C II] observations, contains contributions from thermal motions of the molecules as well as turbulent motions. Therefore, the velocity dispersion values were corrected as  $(\delta V_t)^2 = (\delta V)^2 - k_B T_{\text{gas}}/m$ , where  $k_B$ ,  $T_{\text{gas}}$ , and  $m$  are the Boltzmann constant, the gas temperature, and the molecule’s mass. In this work, we assume 30 Dor is in LTE condition and adopt  $T_{\text{gas}} = T_{\text{ex}}$ . We computed the excitation temperature  $T_{\text{ex}}$  at each pixel using its maximum main-beam temperature as in Pineda et al. (2008).

According to Guerra et al. (2021), there are two alternatives to fitting the dispersion function (see their Appendix A): (1) One can solve for all three parameters ( $a_2$ ,  $\langle B_t^2 \rangle / \langle B_0^2 \rangle$ ,  $\delta$ ) simultaneously. If this provides the majority of pixels in the map with values of  $\delta$  greater than  $\sqrt{2}W$ , then the turbulent contribution is well resolved by the polarimetric observations, and the values of  $\langle B_t^2 \rangle / \langle B_0^2 \rangle$  are well defined. (2) If the condition  $\delta > \sqrt{2}W$  is not met for the majority of pixels, the parameter  $\delta$  can be fixed to a prescribed value, and the MCMC solver computes only two parameters,  $a_2$ ,  $\langle B_t^2 \rangle / \langle B_0^2 \rangle$ . For this investigation, the first approach was tried with all polarimetric maps, but only the 214  $\mu\text{m}$  satisfied the condition mentioned above. For the results here presented, we used the second approach, with a prescribed  $\delta$  value for each pixel equal to that from the global analysis (e.g., when only one dispersion function is calculated for the entire observation). Using the  $\delta$ -fixed approach results in underestimated values of  $\langle B_t^2 \rangle / \langle B_0^2 \rangle$  and overestimated values of  $B_{\text{POS}}$ . However, a test performed with the 214  $\mu\text{m}$  data (the only map for which  $\delta > \sqrt{2}W$  was met in the majority of pixels) showed that differences in  $B_{\text{POS}}$  values using these two approaches were small, with an average value of  $\sim 16\%$ .

The resulting maps of  $B_{\text{POS}}$  strength, calculated using the [C II] data, are presented in Figure 10 for all three bands 89, 154, 214  $\mu\text{m}$  (from the top to bottom). These maps have angular resolutions of  $33''$ ,  $58''$ ,  $77''$ , respectively. The estimated strengths show a dependency with the wavelength of the polarimetric data. The values range between few and  $\sim 350$ ,  $\sim 450$ , and  $\sim 600 \mu\text{G}$  for 214, 154, and 89  $\mu\text{m}$ . This wavelength discrepancy should be mainly because of the angular resolution of the map—shorter wavelengths have smaller resolution. However, there is also a possibility that such differences are the result of each individual wavelength tracing different layers of the cloud. At the same wavelength, the strength structure using CO is similar to the one using [C II], but the amplitudes are slightly lower (see Figure 16, Appendix B). The uncertainty of our calculation is discussed in Section 4.5. The black contours in Figure 10 indicate the spatial area in which  $I/\sigma_I \geq 100$ , and  $p/\sigma_p \geq 3$  (e.g., the polarization measurement is statistically significant and intrinsically associated with the source as discussed in Paper I).

<sup>21</sup> Spearman, nonlinear, rank correlation. Values range between 1 and  $-1$ , with the former signaling a perfect correlation.

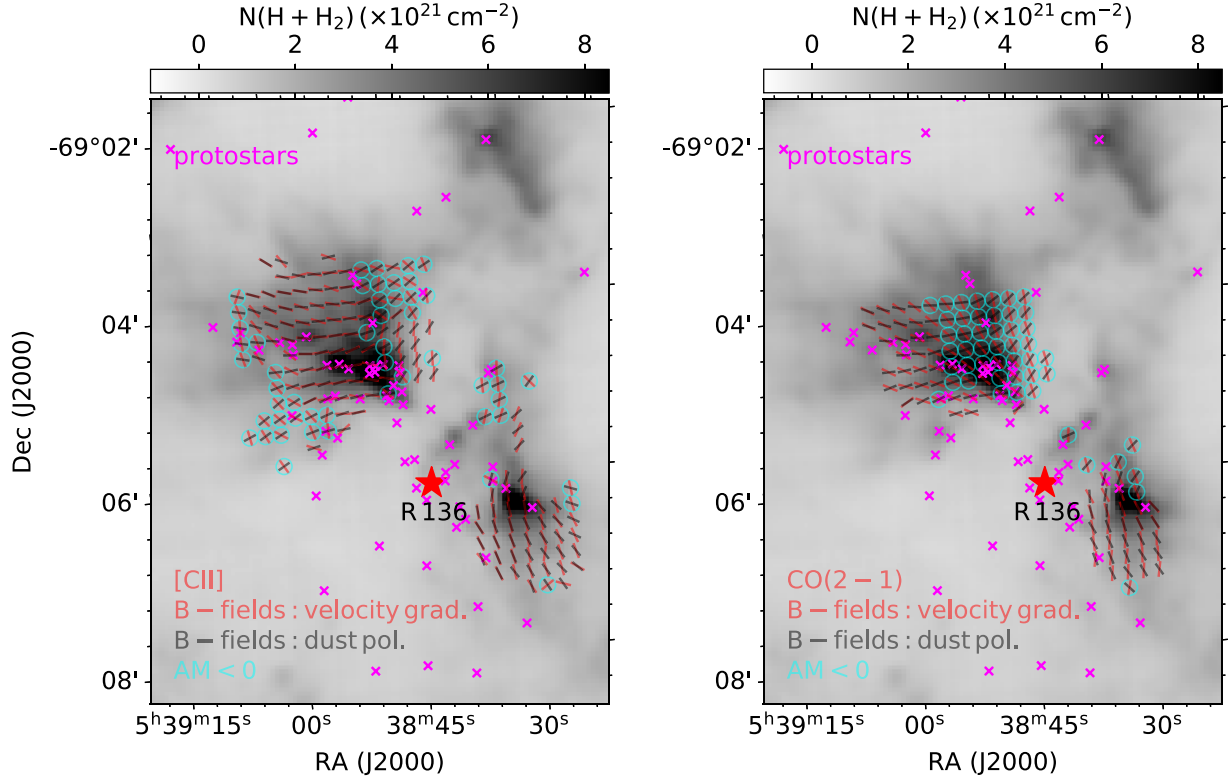


**Figure 8.** Same as Figure 7 but overlaid with the protostars adopted from Indebetouw et al. (2009). Interestingly, the protostars likely locate at the regions where VGTs misalign with  $B$ -fields (i.e., VGs are parallel to the field lines).

### 3.3. Magnetic Fields versus Gravity

An important factor indicating the influence of the  $B$ -field is the mass-to-flux ratio. We adopt the ratio as in Crutcher et al. (2004) as

$$\lambda = 7.6 \times 10^{-21} \frac{N(\text{H}_2)}{B_{\text{tot}}}, \quad (4)$$

where  $B_{\text{tot}} = \sqrt{B_{\text{POS}}^2 + B_{\text{LOS}}^2}$  in  $\mu\text{G}$  is the total  $B$ -field strength in 3D, which is missing in this work because we do not have the LOS component of the field, and  $N_{\text{H}_2}$  in  $\text{cm}^{-2}$  is the gas column density. Statistically,  $\bar{B}_{\text{tot}}$  could be approximated as  $4/\pi \times \bar{B}_{\text{POS}}$  (Crutcher et al. 2004). Using the measured Zeeman LOS component of the field, Guerra et al. (2021) showed that  $B_{\text{tot}} \simeq B_{\text{POS}}$  in the specific case of Orion Molecular Cloud (OMC-1; see their Equation (11)). Lacking information on the LOS component, we simply adopt  $B_{\text{tot}} = B_{\text{POS}}$  with the same caveat as many other studies (e.g., Soam et al. 2018b; Eswaraiah et al. 2021; Hoang et al. 2021b; Ngoc et al. 2021). The gas column density is derived by a modified blackbody fitting from Herschel data at 100, 160, 250, 350, and 500  $\mu\text{m}$  (Meixner et al. 2013) as in Paper I. The cloud is called supercritical for  $\lambda > 1$ , in which the  $B$ -field is insufficient to provide support against the gravitational potential. Otherwise, the cloud is called subcritical for  $\lambda < 1$  in which the  $B$ -field prevents the cloud from collapsing.

Figure 11 (left panels) shows the maps of the mass-to-flux ratio for all three bands (from top to bottom) overlaid with the field lines using [C II]. The similar maps estimated by CO are

**Table 3**

Mean Values of  $\bar{b} \simeq 1$  in Both North and South Regions Indicates That the Turbulence in 30 Dor Is Likely the Compressive Driven

Band	Turbulent Driving Force				
	$\bar{T}_{\text{gas}}$	$\bar{\mathcal{M}}_{\text{A}}$	$\bar{\sigma}_v$	$\sigma$	$\bar{b}$
North Region					
C	31.68	0.41	8.46	0.608	1.15
D	31.68	0.46	8.46	0.608	1.03
E	31.68	0.61	8.46	0.608	0.78
South Region					
C	30.68	0.56	7.60	0.535	0.73
D	30.68	0.52	7.60	0.535	0.78
E	30.68	0.62	7.60	0.535	0.66

shown in Figure 16, (right panels.). Generally, the cloud is subcritical ( $\lambda < 1$ ) for most of the region, except at the peak intensity in both the north and south ( $\lambda \geq 1$ ), and the regions where  $\lambda \sim 1$  spreads larger in area at longer wavelengths. Since  $\lambda \sim N(\text{H}_2)$ , and  $B_{\text{pos}} \sim \sqrt{N(\text{H}_2)}$ , the gas density is the main uncertainty factor, which is discussed in Section 4.5. Our derivation of  $N(\text{H}_2)$  agrees quite well with the one from photodissociation region (PDR) models (Chevance et al. 2020). As the maximum of gas column density is about  $10^{22} \text{ cm}^{-2}$ , a hundred  $\mu\text{G}$   $B$ -field can make  $\lambda < 1$  (see Equation (4)).

### 3.4. Magnetic Fields versus Turbulence

The interplay between the  $B$ -field and turbulence can be defined through the Alfvénic Mach number. Because the DCF

assumes that the turbulent magnetic energy balances the turbulent kinematic energy, the total magnetic energy estimated by the DCF method is always greater than the turbulent kinematic energy, which leads to an Alfvénic Mach number that is always lower than 1. Therefore, we use the 3D Alfvénic Mach number to assess the relative importance between the  $B$ -field and turbulence as

$$\mathcal{M}_A = \sqrt{3} \frac{\sigma_{\text{NT}}}{\mathcal{V}_A}, \quad (5)$$

where  $\sigma_{\text{NT}}$  is the nonthermal velocity dispersion, and  $\mathcal{V}_A = B_{\text{tot}}/\sqrt{4\pi\rho}$  is the Alfvénic velocity.  $\mathcal{M}_A < 1$  stands for the sub-Alfvénic, the impact of the gas turbulence is minimal, and the  $B$ -fields is able to regulate the gas motion.  $\mathcal{M}_A > 1$  stands for the super-Alfvénic; the gas turbulence drives the  $B$ -field to be random.

The right panel in Figure 11 shows the maps of the Alfvénic Mach number in three bands (from top to bottom) using [C II], while the ones using CO are shown in the left panels of Figure 17. These maps are color scaled such that the blue color represents  $\mathcal{M}_A < 1$ , and the red color is for  $\mathcal{M}_A > 1$ . One can see that the entire cloud is made up of sub-Alfvénic motions, while it is trans- or super-Alfvénic at around the peaked intensity both in the north and south, except at  $214 \mu\text{m}$  where the south peak becomes sub-Alfvénic. Similar to mass-to-flux ratio maps, the trans-Alfvénic area is more widespread at longer wavelength.

The magnetic and isotropic turbulent pressures in units of dyn per square centimeter are computed as

$$\begin{aligned} P_{\text{mag}} &= \frac{B_{\text{tot}}^2}{8\pi}; \\ P_{\text{turb}} &= \frac{3}{2} \rho (\sigma_{\text{NT}})^2. \end{aligned} \quad (6)$$

If  $P_{\text{turb}}/P_{\text{mag}}$  is greater than 1, the turbulence pressure is higher than the magnetic pressure; otherwise the magnetic pressure is dominant. The maps in all three bands are shown in the left panels of Figure 12, indicating that the turbulent pressure is comparable and higher than that of the  $B$ -field at which  $\mathcal{M}_A \gtrsim 1$ ; elsewhere it becomes lower (see Figure 11, right panels). The similar trends are seen using CO as shown in Figure 17, right panels.

### 3.5. Magnetic versus Thermal Pressure

The relative importance between the magnetic and thermal pressure could be quantified through a so-called plasma beta parameter, which is a ratio of these two pressures as

$$\beta = \frac{P_{\text{thermal}}}{P_{\text{mag}}} = \frac{2c_s^2}{\mathcal{V}_A^2}, \quad (7)$$

where  $c_s = \sqrt{k_B T_{\text{gas}}/\mu_{\text{H}_2} m_{\text{H}}}$  is the thermal sound speed. Figure 12, right panels, shows the maps of the thermal to magnetic pressure ratio. The magnetic pressure is much stronger than the thermal one and varies across the cloud, which is confirmed by the constraints observed by Lee et al. (2019), Chevance et al. (2020) using the PDR Meudon code. Indeed, the authors constrained that  $P_{\text{thermal}} \sim 10^4\text{--}10^6 \text{ K cm}^{-3}$ , while we showed that  $P_{\text{mag}} \sim 10^7\text{--}10^8 \text{ K cm}^{-3}$ , with  $B = 200\text{--}500 \mu\text{G}$ .

## 4. Discussions

### 4.1. Gas Column Density Probability Distribution and Turbulent Driving Force

The interplay between the gravity, magnetic fields, and turbulence in the star formation has been raised and discussed in numerous studies. The probability distribution function (PDF) of the gas column density was demonstrated to be a key to study the dynamics of molecular clouds. The PDF density of the isothermal and non-self-gravity gas follows closely a log-normal distribution; while this PDF develops a power-law tail once the self-gravity dominates, and the collapse is significant (e.g., Klessen 2000; Federrath & Klessen 2013; Schneider et al. 2013, 2015, 2022; Girichidis et al. 2014; Kainulainen et al. 2014).

However, the shape of the PDF strongly depends on the way observations are performed as studied in Körtgen et al. (2019). The authors demonstrated that a small or insufficient field of view will result in a cut-off in the log-normal part of the distribution, and argued that a sufficiently large field of view is needed for the PDF to be built completely. Thus, we used the whole column density map to build the PDF in Figure 13. Then, we fit a log-normal to the histogram as shown by the solid lines. One can see that a log-normal could not fit entirely the PDFs of both the north's and south's gas density, but up to  $S_f \simeq 0.657$ , or  $N \geq 1.8 \times \bar{N}_{\text{North}} = 3 \times 10^{21} \text{ cm}^{-2}$  in the north (upper panel), and  $S_f \simeq 1.239$ , or  $N \geq 3.5 \times \bar{N}_{\text{South}} = 3.8 \times 10^{21} \text{ cm}^{-2}$  in the south (lower panel). Above these values, power-law tails can be seen in both regions. This reveals that the gravitational instability likely sets in relatively low gas density in 30 Dor cloud in general, and the north experiences it at a slightly lower density than that of the south because its power-law tail pops up earlier. The gravitational collapse in parsec scale has been proposed in various studies (e.g., Hartmann & Burkert 2007; Peretto et al. 2006, 2013; Schneider et al. 2010; Jackson et al. 2019; Bonne et al. 2022b). Another note is that the gravitational collapse in the south is much more compact than that in the north.

Figure 8 shows the location of the protostars candidates adopted from Indebetouw et al. (2009). These locations span from low to the peak gas column density. Interestingly, the protostars' locations are coincident with the misaligned vectors between the rotated VGs by [C II] and CO and the  $B$ -fields, or at which these gas motions are parallel to the field lines.

The power-law tails have been seen to develop even in low column density gas, and we suspect that the turbulence could be the key gradient to make that happened. There are three main turbulent types, i.e., compressive (curl-free), solenoidal (divergence-free), and the mixing, in which the compressive turbulence results in stronger compression and thus larger deviation of the PDF (Federrath et al. 2010). These three types of turbulence could be identified through the turbulence driving parameter  $b$  defined as

$$b^2 = \frac{e^{\sigma^2} - 1}{M_S^2} \frac{\beta + 1}{\beta}, \quad (8)$$

where  $M_S$  is the sonic Mach number,  $\sigma$  is the standard deviation of the log-normal distribution in Figure 13,  $\beta = 2M_A^2/M_S^2$  is the compressibility (or the plasma beta parameter in the right panel of Figure 12) with  $M_A$  as the Alfvénic Mach number. Purely solenoidal driving has  $b = 1/3$ , the compressive driving turbulence yields  $b = 1$ , and a stochastic forcing mixture has

$b \sim 0.4$  (Federrath et al. 2010). Table 3 shows the mean values in the north and south regions. One can see that  $b \simeq 1$  in both regions, which indicates that the driving force of turbulence in 30 Dor is mainly compressive. This is consistent with the existence of the supersonic expanding-shells within the cloud discussed in Section 2.3, and similar to other star-forming regions; such as Serpens cloud (Hu et al. 2021).

#### 4.2. Can Star formation Occur Even in the Strongly Magnetized Environment of 30 Doradus?

Figures 8 and 14 show that the VGs of both C II and CO misalign with the  $B$ -fields at certain locations in both north and south regions, which indicates that (1) gas moves parallel to the field lines, and (2) there is gravitational collapse. However, these positions distribute from low to maximum gas density, and mostly in magnetically subcritical, sub-Alfvénic regions where the magnetic pressure is higher than that of the turbulence and thermal. The PDF of gas density in Figure 13 illustrates the power-law tail, an indicator of star formation activities, at not very dense gas (column density few times higher than  $10^{21} \text{ cm}^{-2}$ ) supporting the local collapse scenario, where protostars candidates are likely to locate. How can we explain the ongoing star formations in strong  $B$ -fields?

The turbulence driving parameters  $b \simeq 1$  (see Table 3) reveal that the turbulence is mainly driven by compressive forcing in 30 Dor. The plasma parameter  $\beta \ll 1$ , (see Figure 12, right panel) shows that the sonic Mach number  $\mathcal{M}_s \gg 1$ , indicating the presence of supersonic turbulence. The supersonic compressive turbulence could create overdense gas in which the gravity gets unstable, and stars can form by directly compressing the gas and/or accumulating the gas along the  $B$ -fields line. The latter will not be affected by the magnetic pressure because this pressure acts preferentially perpendicular to the field lines. As a result, the supersonic compressive turbulence could help to trigger the gravitational collapse. That turbulence could result from the cluster-wind from R136 (Melnick et al. 2021) or probably the interaction with much larger giant H I-bubbles in the LMC (Kim et al. 1999). After that, the  $B$ -fields get amplified and slow down the star formation activities, as we observe today.

#### 4.3. Role of Magnetic Fields in Holding 30 Dor Integrity?

30 Dor contains a spectacular feature with multiple large expanding-shells (see Figure 1). The kinematic of these structures is just about  $10^{50}$ – $10^{51}$  erg (Chu & Kennicutt 1994), which could be generated by a cluster-wind (Melnick et al. 2021) or a combination with supernovae (Chu & Kennicutt 1994) from R136. Melnick et al. (2021) estimated the virial mass within a distance of 25 pc from R136 as a few times of  $10^6 M_\odot$ , which is larger than the mass of 30 Dor gas (a few times of  $10^5 M_\odot$ ). Pellegrini et al. (2011) demonstrated that the thermal pressure (in order of  $10^{-9} \text{ dyn cm}^{-2}$ ) is about 1.6 times lower than that of the radiation pressure (see their Figure 18), and is about 3 times higher than the hot gas pressure (i.e., the hot gas pressure is higher elsewhere; see their Figure 21). Thus, how can the 30 Dor cloud survive?

We suspect that  $B$ -fields play a crucial role here in holding the cloud integrity. The  $B$ -field morphology orients perpendicular to the radiation direction, so that the magnetic pressure could resist pressure coming from this direction. Indeed, the

magnetic pressure is  $P_{\text{mag}} \simeq 1.6 \times 10^{-9}$ – $10^{-8} \text{ dyn cm}^{-2}$  for  $B = 200$ – $500 \mu\text{G}$ , which is absolutely higher than both thermal and radiation pressure and thus is capable to resist against the radiative impact. This calculation is in agreement with the right panel in Figure 12. The role of  $B$ -fields could be deduced from a kinematic point of view. Melnick et al. (2021) showed that the kinematic energy of the region within 25 pc from R136 is about 24% the total kinematic energy (which is equivalent to  $\simeq 5 \times 10^{50} \text{ erg}^{22}$ ). For  $B = 200$ – $500 \mu\text{G}$ , the magnetic energy is orders of magnitude larger as  $\simeq 10^{51}$ – $2 \times 10^{52} \text{ erg}$  within the same spherical volume. In addition, Melnick et al. (2021) showed the turbulent kinematic energy could be up to  $10^{51} \text{ erg}$ ; thus, the turbulence only dominates over the  $B$ -fields for  $B < 200 \mu\text{G}$ , which is consistent with the maps of  $\mathcal{M}_A$  (right panel in Figure 11) and  $P_{\text{turb}}/P_{\text{mag}}$  (left panel in Figure 12).

The next question could be how large external shells developed around our cloud? 30 Dor opens to the eastern direction from R136, which helps hot gas (traced by X-ray; see Figure 14 in Townsley et al. 2006) easily escape and creates the large expanding-shell along this direction. The mechanism could otherwise be complicated along other directions, especially northern and western. There are multiple expanding-shells on a smaller scale within the cloud (see Figure 6) referring to the fact that the cloud is being carved by the cluster feedback. Melnick et al. (2021) proposed that this impact could lead the certain cloud’s structure to break, which enables hot gas to go through and “inflate” the external expanding-shells along these directions. Interestingly, Figure 10 shows that the  $B$ -field strength is relatively weak (i.e., lower than  $200 \mu\text{G}$ ) at certain regions in 30 Dor along directions that point to or adjoin to these external structures. Along these directions, the field is insufficient to resist feedback; thus, there are nozzles where the hot gas can escape through the cloud.

#### 4.4. Comparison with the Larger-scale Magnetic Field of the Hosting LMC

The larger-scale  $B$ -fields have been measured using both near-infrared (NIR; e.g., Nakajima et al. 2007; Kim et al. 2016) and radio polarimetric observations (e.g., Klein et al. 1993; Mao et al. 2012).

The absorption polarization at NIR probed the  $B$ -field structure outside our region (see Figure 3 in Nakajima et al. 2007). These large field lines are seen to associate with the dust cloud in LMC and the large expanding-structures around 30 Dor. The  $B$ -field strength from this more diffuse region was estimated of 3–25  $\mu\text{G}$  using DCF.

The  $B$ -fields measured by synchrotron polarized emission inferred the larger scale of LMC. The low spatial resolution (e.g.,  $14'$  in Mao et al. 2012) was unable to resolve our region. The total  $B$ -field strength is measured  $< 7 \mu\text{G}$ , assuming equipartition with cosmic-ray electrons, with an upper-limit  $B_{\text{POS}}$  of 11  $\mu\text{G}$  in the H I southwestern filaments up to the 30 Dor region. The higher  $B$ -field strength in the filaments may be due to anisotropic turbulent  $B$ -fields mostly located in the plane of sky.

Our maximum  $B$ -field strengths of 350–600  $\mu\text{G}$  at parsec scales using thermal dust polarization are much higher than those from the NIR and radio polarimetric observations in more

<sup>22</sup> Numeric values are adopted from Table 3 in Melnick et al. (2021).

diffuse media, which may be enhanced due to turbulent dynamo mechanism and star formation activity. The additional larger FIR and higher spatial resolution radio polarimetric observations of the LMC are required to better understand the connection between galactic  $B$ -fields and those  $B$ -fields responsible for the star formation activity and molecular cloud formation.

#### 4.5. Uncertainties

In this section, we discuss several possible uncertainties. Our first concern lies in the estimate of the column density, which is constructed by the modified spectral energy distribution fitting from Herschel data (see Paper I). Our derived column density agrees well in a range of  $1.9 \times 10^{21} - 1.3 \times 10^{22} \text{ cm}^{-2}$  estimation from PDR modeling (Chevance et al. 2020), but  $1.3 \times 10^{22} \text{ cm}^{-2}$  is 1.12 times higher than our maximum derivation. Hence if  $B_{\text{pos}} \sim N(\text{H}_2)^{0.5}$ , the mass-to-flux ratio  $\lambda$  increases by a factor 1.06, and the Alfvénic Mach number correspondingly decreases by a factor of 0.94, the magnetic pressure increases by a factor of 1.12. The values are slightly changed but do not affect our conclusions.

Our second concern is related to the volume density derived from the column density. The depth of the cloud is fixed and estimated by the autocorrelation function from the polarized intensity. Thus, our derived volume density is insensitive to the local cloud depth, which could be either overestimated or underestimated.

The third concern is the nonthermal velocity dispersion. We computed this term by using [C II] and  $^{12}\text{CO}$  emission lines. These lines are not necessarily optically thin and show multiple components; hence it is not ideal for probing the turbulence component of the gas motion even though it shows no evident signs of absorption. If these emissions are optically thick, the nonthermal velocity dispersion might be overestimated because  $(\delta V_{\text{turb}})^2 \sim (\delta V)^2$  (e.g., Phillips et al. 1979; Hacar et al. 2016).

The fourth concern is the gas temperature, because  $(\delta V_{\text{turb}})^2 \sim (\delta V)^2 - k_B T_{\text{gas}}/m_{\text{gas}}$ . We assume the gas is in the LTE condition, so we adopt  $T_{\text{gas}} = T_{\text{ex}}$  across the entire cloud. This assumption will fail at the locations where the LTE is simply incorrect. However, we expect that  $T_{\text{gas}}$  has a little impact on the final result because (1) the thermal contribution is relatively small ( $\simeq 2.6 \text{ km s}^{-1}$ , for  $T_{\text{gas}} = 10^4 \text{ K}$ ) compared to the total velocity dispersion (Figure 5), and (2) this velocity dispersion is supersonic for [C II].

The fifth concern is the strength of the  $B$ -field in 3D space. In this work, we adopt the value of the POS component of  $B$ -field since its LOS component is unknown in 30 Dor. The higher value of the total  $B$ -field strength will result in lower values of  $\lambda$ ,  $\mathcal{M}_A$ , while increased in  $P_{\text{mag}}$ . Chen et al. (2019) proposed a method to estimate the inclination of  $B$ -fields by assuming uniform  $B$ -fields (i.e., no variation in position angle and inclination of the field lines) and a constant polarization coefficient (i.e.,  $p_0$  in their Equation (10)) throughout a cloud. These assumptions are unlikely to be satisfied in the case of 30 Dor given a variation of the field lines and the polarization degree across the cloud.

The sixth concern is the method to estimate the  $B$ -field strength. In this work, we use an improved version of the DCF method from Houde et al. (2009), in which the structure-function of polarization angle is used rather than the dispersion function of this quantity. Skalidis & Tassis (2021), Skalidis et al. (2021) showed that the strength of the

mean  $B$ -field component is proportional to  $1/\sqrt{\delta\phi}$ , which is different from Equation (2). However, this approach assumed an equipartition between turbulent motions and the parallel component of turbulent  $B$ -fields whose physical basics behind it is not clear (see Appendix A3 in Li et al. 2022; and Section 10.3 in Lazarian et al. 2022). Recently, at the time of this work, Lazarian et al. (2022) proposed a new method to estimate the field strength, namely DMA as  $B \simeq f \sqrt{4\pi\rho} D_v^{1/2} / D_\phi^{1/2}$  where  $D_v$ ,  $D_\phi$  are the structure-functions of the velocity centroids and polarization angle, and  $f$  is the factor based on the anisotropic turbulence. The authors showed that the DMA method could estimate the field strength at the smallest scale (lower than the turbulence injection scale) and with anisotropic turbulence properties. These two modifications contrast the DCF method and could increase the estimation accuracy. A comparison between DCF and DMA is beyond the scope of this work, and it hence serves as an important improvement for future works (not only for 30 Dor but also other star formation regions).

To summarize, the quantitative value of  $B$ -field strengths could be different from what is presented in this work once using a proper value of the nonthermal velocity dispersion and the gas temperature for the DCF or different methods. However, it could not change by orders of magnitude, and we do not expect it will change the effect of the  $B$ -field. Indeed, when the strength is as high as hundreds of  $\mu\text{G}$ , the field is strong enough to support against the gravitational potential (Equation (4)) and is sufficient to resist the hot gas and radiation pressures (Section 4.3).

## 5. Conclusions

The entire 30 Dor is a complex star-forming region, which clearly shows a core-halo structure, in which there are multiple parsec-scale expanding-shells structures in the outer region and a cloud in the inner region. Cluster-wind or a combination of supernovae from the star cluster R136 is demonstrated to be the main source of energy for these giant-shells (Chu & Kennicutt 1994; Melnick et al. 2021). However, it is not very clear how an inner structure is able to remain close to this source of energy. Thus, we study the gas kinematics and  $B$ -fields in this region in this work, for which we use the same name as 30 Dor for the sake of convenience. Our main findings are summarized as follows.

1. We derived the  $B$ -field morphology from thermal dust polarization observed by SOFIA/HAWC+, which shows the highly ordered yet complex  $B$ -field structure. The field lines are wrapped and bent around the peak intensity (where the gas is densest, Figure 9). The tip of the bending fields points toward the star cluster, R136.
2. We performed a velocity field analysis on two different gas tracers. One is expected to trace warmer and more diffuse gas ([C II]), and the other is expected to trace cold and dense gas (CO). Our analysis indicates a complex dynamic structure but organized with multiple gas components and wing-like structures. The change from the blueshifted to redshifted gas is directly related to the  $B$ -field morphology change. Furthermore, the position-velocity diagrams showed possible multi expanding-shells in 30 Dor.

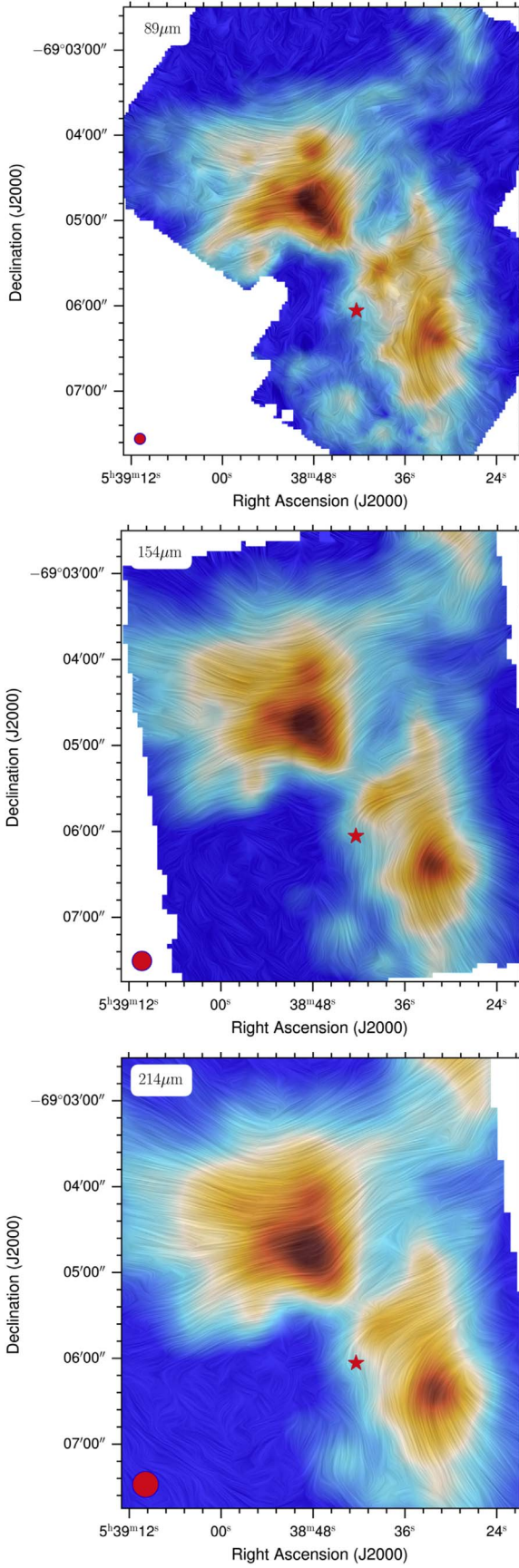


**Figure 9.** Magnetic field morphology in 30 Dor for all three bands (from top to bottom). The background is the total intensity Stokes I. Streamlines are the Local Interstellar Cloud (Cabral & Leedom 1993). The Star symbol indicates the R136 location.

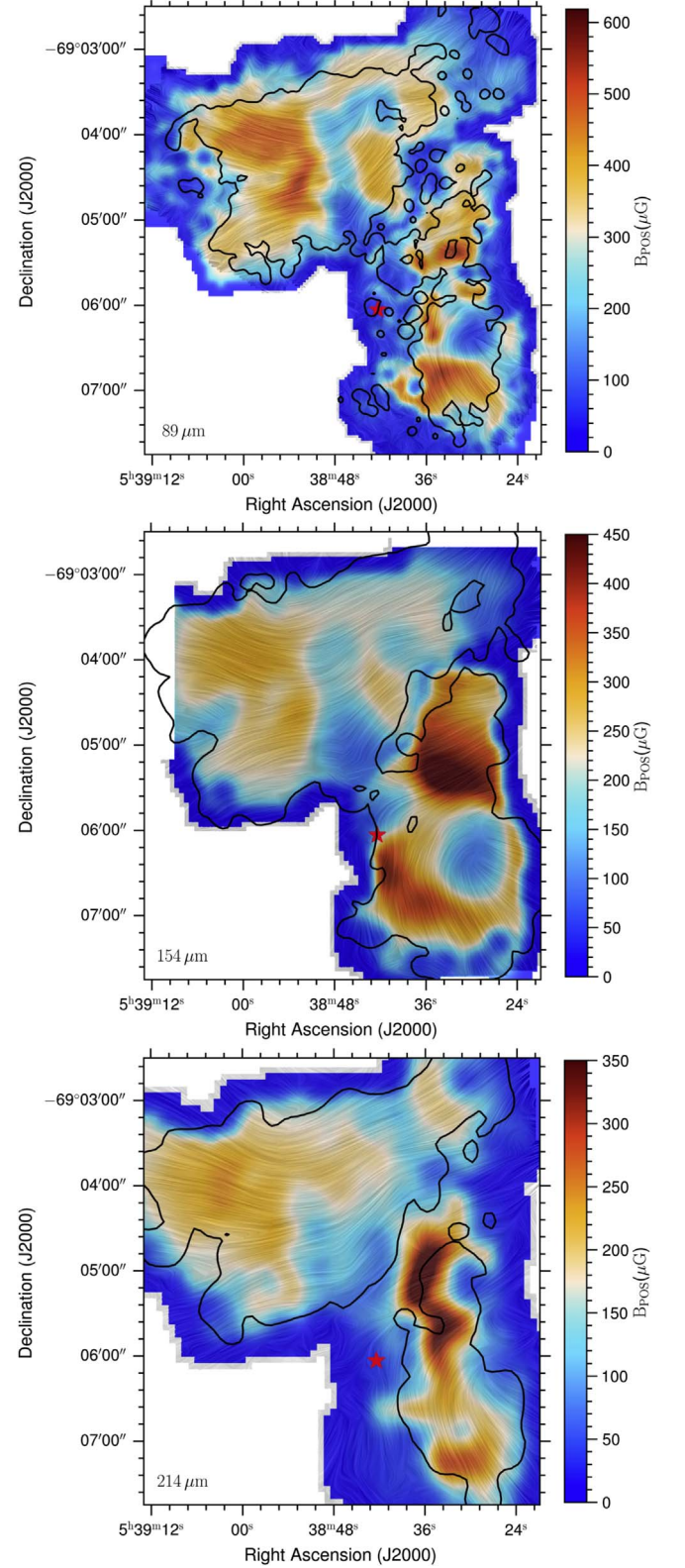


**Figure 10.** Maps of  $B_{POS}$  strength for all three bands (from top to bottom) using [C II] overlaid with the  $B$ -field orientation. The black contours indicate the region where  $I/\sigma_I \geq 100$ , and  $p/\sigma_p \geq 3$ . The star symbol indicates the R136 location. The  $B$ -field strength is weaker at longer wavelengths with peaks offset from the total intensity.

3. We compared the  $B$ -fields obtained using the VGT of both [C II] and CO and showed that the  $B$ -fields mostly align with the one inferred from thermal dust polarization

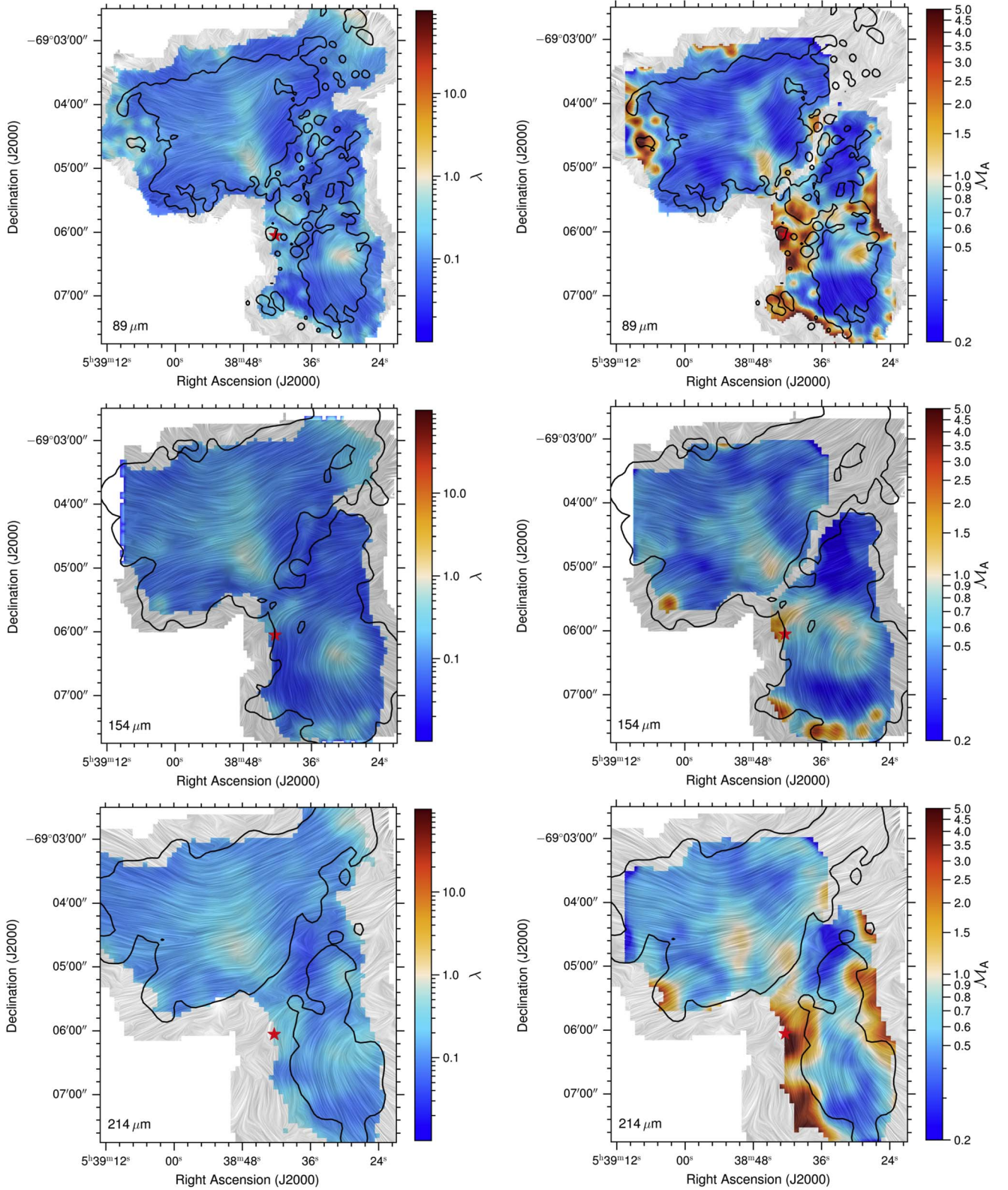


**Figure 11.** Maps of the mass-to-flux ratio (left panels), and the Alfvénic Mach number (right panels) for all three bands (wavelength increases from top to bottom) overlaid with the fields morphology. The black contours' border is defined where  $I/\sigma_I \geq 100$ , and  $p/\sigma_p \geq 3$ . The red star indicates the R136 location.

observed by SOFIA/HAWC+ in the south, while in the north numerous misalignment vectors are seen (Figure 7). CO line shows antialignment at dense gas, and C[II] complementary illustrates the misalignment at more diffuse regions.

4. The misalignment between the  $B$ -fields induced by the VGT and the thermal dust polarization evidences the local gravitational collapse because it could pull the gas along the fields; the VGs are thus parallel rather than perpendicular to the field lines.

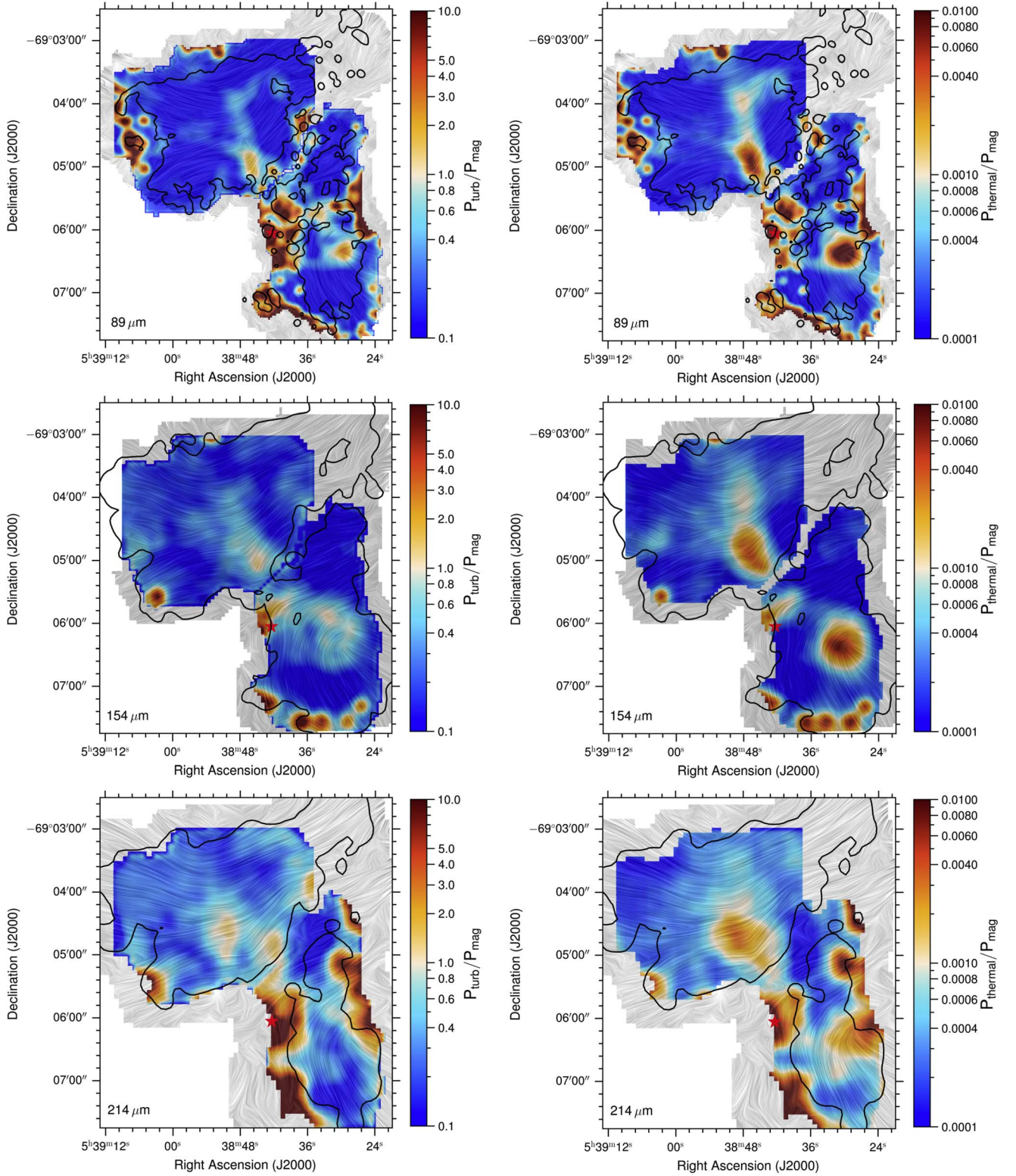


**Figure 12.** Turbulent-to-magnetic pressure ratio (left panels) and thermal-to-magnetic pressure ratio (right panels). The symbols are the same as in Figure 11. The magnetic pressure is higher than that of the turbulence everywhere across the cloud except in the peak intensity and the eastern edge in the north where the turbulent pressure is higher or comparable to the magnetic pressure at the peak intensity in the north and south regions. The magnetic pressure is dominating the thermal one over the cloud.

5. We showed that the PDF of the gas column density (Figure 13) exhibits a power-law tail, which is a sign of gravitational collapse. This is consistent with the constraints of the VGs.

6. We estimated the  $B_{\text{POS}}$  using the DCF method. Our estimation shows that the  $B$ -fields are quite strong in 30 Dor with maxima of 600, 450, and 350  $\mu\text{G}$  at 89, 154, and 214  $\mu\text{m}$ , respectively (Figure 10). Thus, 30 Dor is

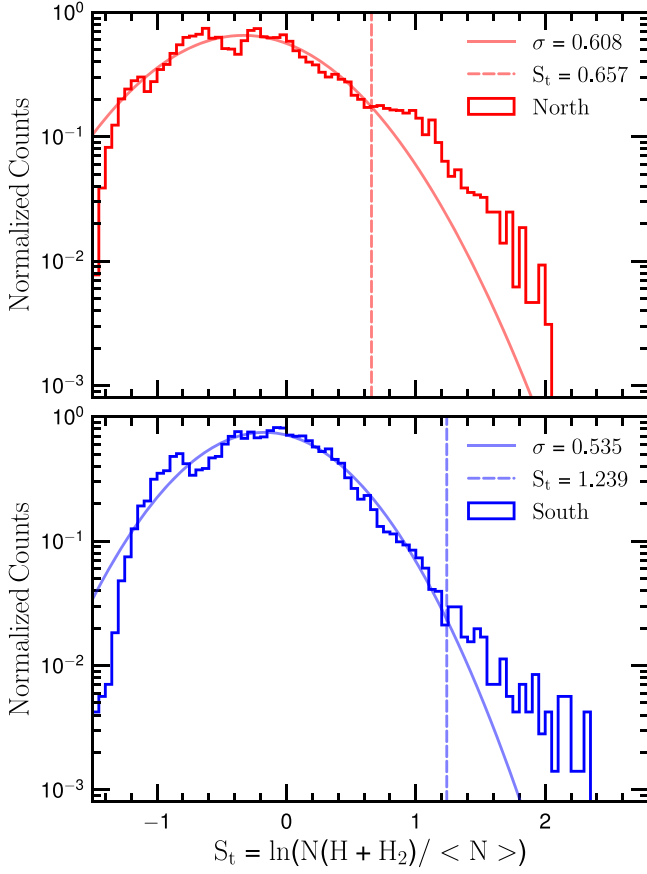


**Figure 13.** PDF distribution of the logarithm of the gas column density in the north (upper) and in the south (lower). A log-normal just fits up to  $S_t \simeq 0.657$  (north) or  $S_t \simeq 1.239$  (south), which are followed by a power-law tail. Apparently, the tail-structure in the north appears at lower gas density than that in the south.

mostly subcritical ( $\lambda < 1$ ; see Figure 11, left panel) and sub-Alfvénic ( $\mathcal{M}_A < 1$ ; see Figure 11, right panels), except at the peak intensity where the gas density is densest. The  $B$ -field is also dominant over the turbulent (Figure 12, left panels), and substantially higher than the thermal contribution (Figure 12, right panels).

7. We found that the turbulence is mainly driven by compressive forcing and is supersonic. We proposed that the supersonic compressive turbulence helps form a new generation of stars in strong  $B$ -fields in 30 Dor by compressing and/or accumulating the gas along the  $B$ -field lines. As the latter is not influenced by magnetic pressure, this process could happen even in the regions where the  $B$ -fields are strong enough to act against the gravitational collapse.

Our considered region is being carved by the R136 feedback resulting in multiple expanding-shells. The  $B$ -fields are sufficiently strong and seem to play a key role in supporting the cloud structure against this stellar feedback. However, there are certain regions at which the  $B$ -fields are relatively weak, where the gas can escape and inflate the external giant-shells. Inside 30 Dor, supersonic and compressive turbulence accumulates gas along the field lines, enabling gravitational collapse and triggering stars' formation in strong  $B$ -fields environments. We argue that future polarimetric observations covering a large area in 30 Dor will

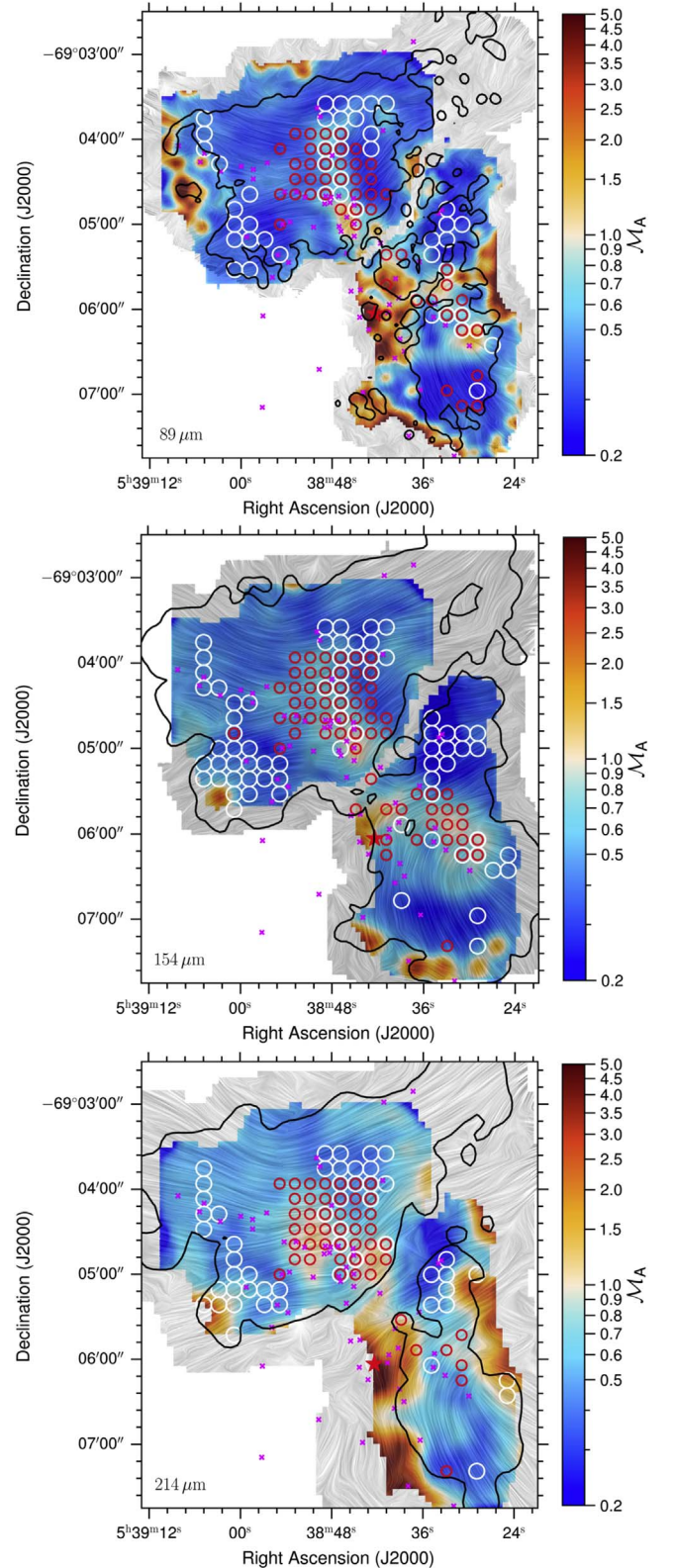


**Figure 14.** Alfvénic Mach number as shown in right panel of Figure 11. The white and red circles mark the positions where VGs from C II and CO are parallel to the fields (i.e., misaligned between VGT and magnetic field lines as shown in Figure 7), respectively. The magenta symbols show the locations of the protostars.

be necessary to better understand the role of  $B$ -fields in the kinematical evolution of the entire 30 Dor region. In addition, the  $B$ -field strength estimated from the thermal dust

polarization of 30 Dor is much higher than the average derived from the diffuse radio polarimetric observations of the hosting LMC. More sensitivity and resolution of polarimetric observations at radio wavelengths are needed to better understand the link from the galactic-scale to cloud-scale  $B$ -fields.

However, we would like to warn the reader that our estimation of  $B$ -field strengths suffers from numerous uncertainties, as discussed in Section 4.5. Consequently, the values of  $B$ -field strengths and other related parameters could vary. Nevertheless, we do not expect our main conclusions on the role of  $B$ -fields will be changed significantly or be reversed.

This research is based on observations made with the NASA/DLR Stratospheric Observatory for Infrared Astronomy (SOFIA). SOFIA is jointly operated by the Universities Space Research Association, Inc. (USRA), under NASA contract NNA17BF53C, and the Deutsches SOFIA Institut

(DSI) under DLR contract 50 OK 0901 to the University of Stuttgart. Financial support for this work was provided by NASA through award 4\_0152 issued by USRA. T.H. is funded by the National Research Foundation of Korea (NRF) grant funded by the Korea government (MSIT) through the Mid-career Research Program (2019R1A2C1087045). A.L. and H. Y. acknowledge the support of NSF AST 1816234, NASA TCAN 144AAG1967, and NASA ATP AAH7546.

Facility: SOFIA.

## Appendix A Channel and Moment Maps of [C II]

Figure 15 shows the channel maps of C II. It demonstrates the presence of relatively complex kinematics in the region. Expanding shell candidates, established based on the PV diagrams of Figure 6, are indicated with red circles in their respective velocity ranges. The channel maps indeed show several curved velocity structures that could be associated with the expanding shells.

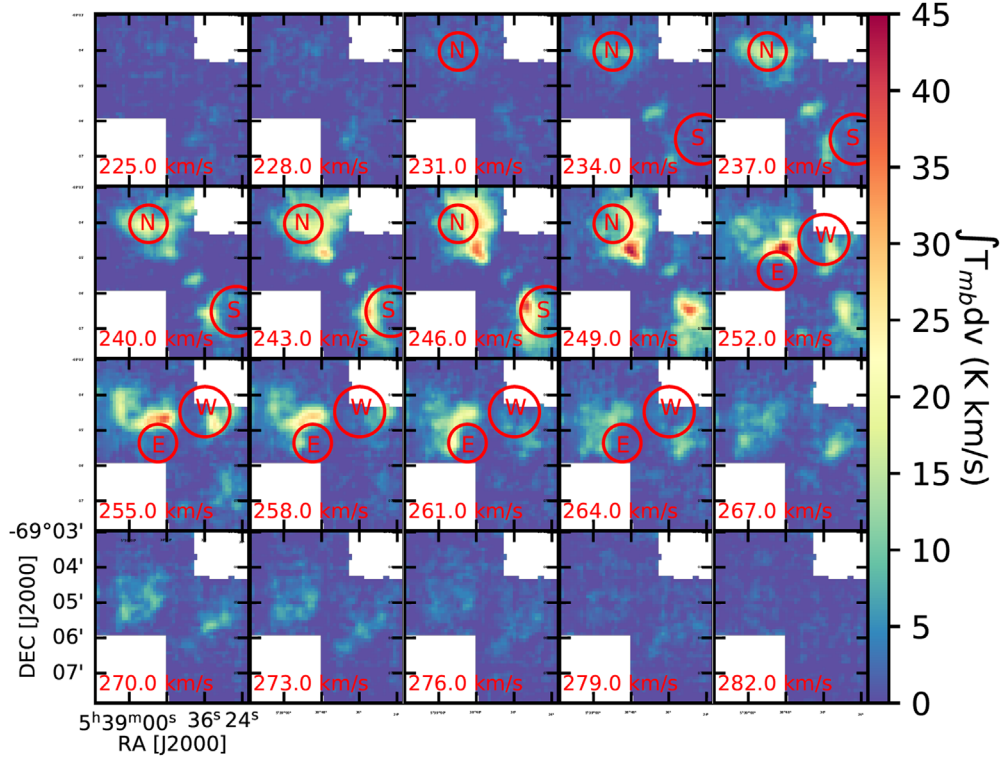
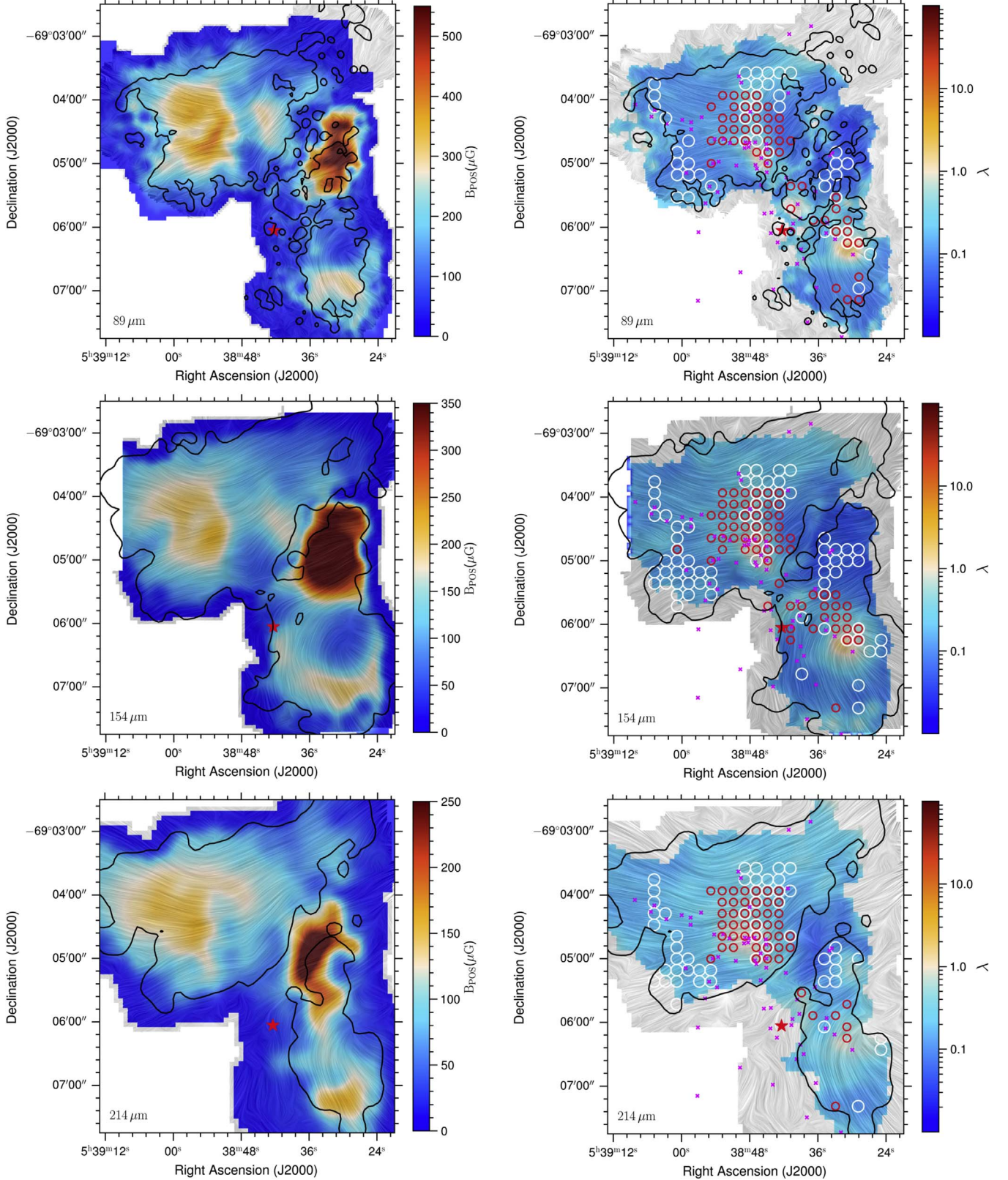


**Figure 15.** Channel maps of the 30 Dor region, in steps of  $3 \text{ km s}^{-1}$ , displaying the [C II] dynamics of the region. The red circles indicate the expanding shell candidates from Table 1 in their proposed velocity with their name.

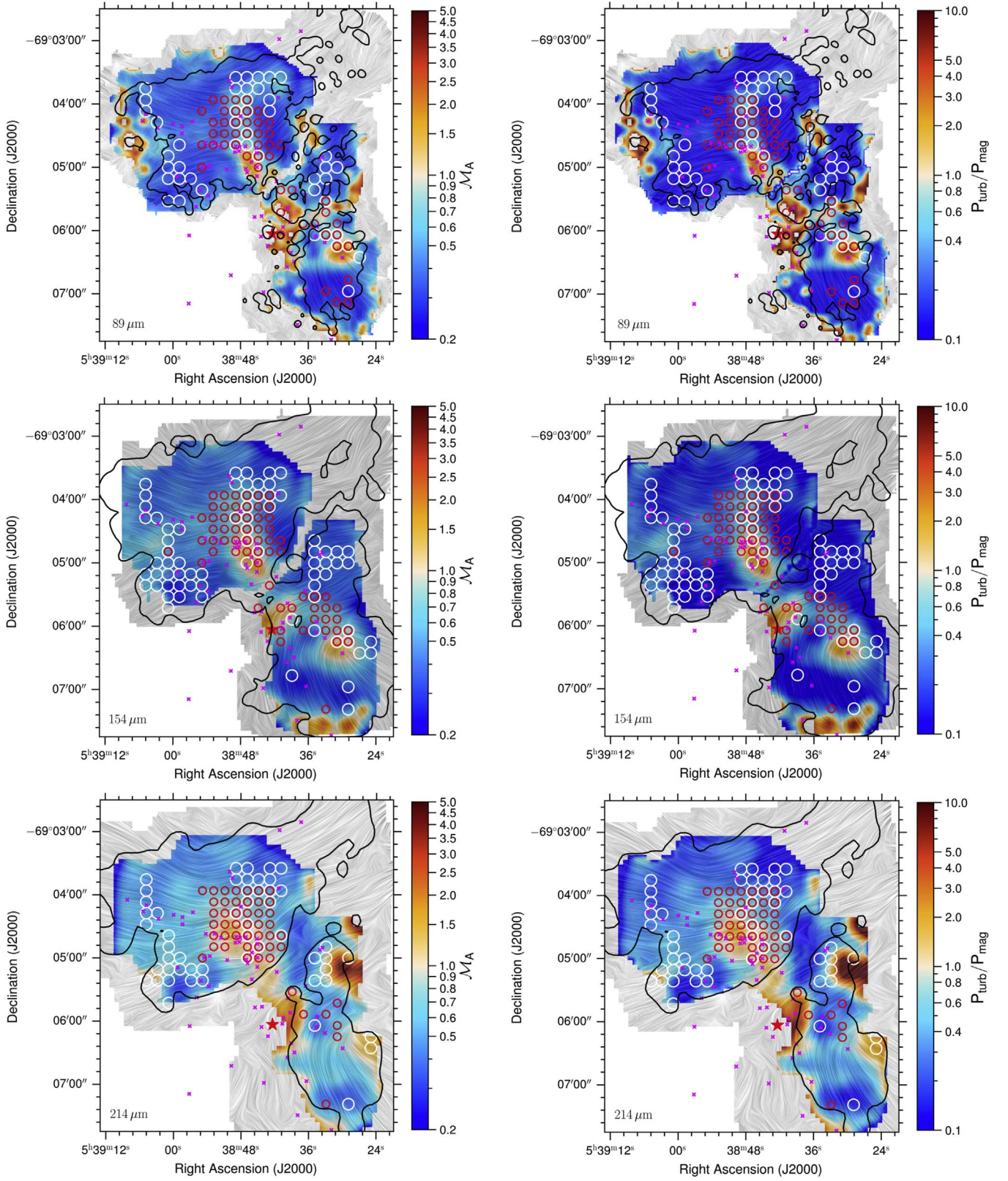
### Appendix B Magnetic Fields Using CO(2-1)

Figure 16, left panel, shows maps of the strength of  $B$ -field estimated using the velocity dispersion from CO(2-1). A

similar structure as in Figure 10 is seen, but the amplitude is slightly lower because of the narrower velocity dispersion of CO(2-1) (see lower panels in Figure 5). Right panels of Figures 16 and 17 show the mass-to-flux ratio, Afvénic Mach

















**Figure 16.** Left:  $B$ -field strength estimated by DCF method similar using CO(2-1) data. Right: mass-to-flux ratio derived by the field strength on the left panel. Symbols are the same as in Figure 11.



**Figure 17.** Afvénic Mach number (left panel) and turbulent-to-magnetic pressure ratio (right panel) derived by the field strength in Figure 16. Symbols are the same as in Figure 11.

number, and turbulence-to-magnetic pressure ratio. As seen in [C II], the magnetic field is sufficiently strong to take over the gravitational potential and turbulence pressure except at the peak intensity.

### ORCID iDs

Le Ngoc Tram  <https://orcid.org/0000-0002-6488-8227>  
 Lars Bonne  <https://orcid.org/0000-0002-0915-4853>  
 Yue Hu  <https://orcid.org/0000-0002-8455-0805>  
 Enrique Lopez-Rodriguez  <https://orcid.org/0000-0001-5357-6538>  
 Jordan A. Guerra  <https://orcid.org/0000-0001-8819-9648>  
 Thiem Hoang  <https://orcid.org/0000-0003-2017-0982>  
 Min-Young Lee  <https://orcid.org/0000-0002-9888-0784>  
 Alex Lazarian  <https://orcid.org/0000-0002-7336-6674>  
 B-G Andersson  <https://orcid.org/0000-0001-6717-0686>  
 Simon Coudé  <https://orcid.org/0000-0002-0859-0805>  
 Archana Soam  <https://orcid.org/0000-0002-6386-2906>  
 William D. Vacca  <https://orcid.org/0000-0002-9123-0068>  
 Hyeseung Lee  <https://orcid.org/0000-0003-3465-3213>  
 Michael Gordon  <https://orcid.org/0000-0002-1913-2682>

### References

- Abe, D., Inoue, T., Inutsuka, S.-I., & Matsumoto, T. 2021, *ApJ*, **916**, 83
- Alina, D., Montillaud, J., Hu, Y., et al. 2022, *A&A*, **658**, A90
- Andersson, B. G., Lazarian, A., & Vaillancourt, J. E. 2015, *ARA&A*, **53**, 501
- Arthur, S. J., Henney, W. J., Mellema, G., de Colle, F., & Vázquez-Semadeni, E. 2011, *MNRAS*, **414**, 1747
- Beuther, H., Schneider, N., Simon, R., et al. 2022, *A&A*, **659**, A77
- Bonne, L., Bontemps, S., Schneider, N., et al. 2020b, *A&A*, **644**, A27
- Bonne, L., Peretto, N., Duarte-Cabral, A., et al. 2022b, *A&A*, **665**, A22
- Bonne, L., Schneider, N., Bontemps, S., et al. 2020a, *A&A*, **641**, A17
- Bonne, L., Schneider, N., García, P., et al. 2022a, *ApJ*, **935**, 171
- Brandl, B. R. 2005, in *Astrophysics and Space Science Library*, Vol. 329, *Starbursts: From 30 Doradus to Lyman Break Galaxies*, ed. R. de Grijs & R. M. González Delgado (Dordrecht: Springer), 49
- Cabral, B., & Leedom, L. C. 1993, in *Proc. of the 20th Annual Conf. on Computer Graphics and Interactive Techniques, SIGGRAPH '93* (New York, NY: ACM), 263
- Chandrasekhar, S., & Fermi, E. 1953, *ApJ*, **118**, 113
- Chen, C.-Y., King, P. K., Li, Z.-Y., Fissel, L. M., & Mazzei, R. R. 2019, *MNRAS*, **485**, 3499
- Chevance, M., Madden, S. C., Fischer, C., et al. 2020, *MNRAS*, **494**, 5279
- Cho, J., & Lazarian, A. 2003, *MNRAS*, **345**, 325
- Chu, Y.-H., & Kennicutt, R. C. J. 1994, *ApJ*, **425**, 720
- Crutcher, R. M. 2012, *ARA&A*, **50**, 29
- Crutcher, R. M., Nutter, D. J., Ward-Thompson, D., & Kirk, J. M. 2004, *ApJ*, **600**, 279
- Davis, L. 1951, *PhRv*, **81**, 890
- Eswaraiah, C., Li, D., Furuya, R. S., et al. 2021, *ApJL*, **912**, L27
- Ewertowski, B., & Basu, S. 2013, *ApJ*, **767**, 33
- Federrath, C., & Klessen, R. S. 2013, *ApJ*, **763**, 51
- Federrath, C., Roman-Duval, J., Klessen, R. S., Schmidt, W., & Mac Low, M. M. 2010, *A&A*, **512**, A81
- Girichidis, P., Konstantin, L., Whitworth, A. P., & Klessen, R. S. 2014, *ApJ*, **781**, 91
- González-Casanova, D. F., & Lazarian, A. 2017, *ApJ*, **835**, 41
- Gordon, M. S., Lopez-Rodriguez, E., Andersson, B. G., et al. 2018, *arXiv:1811.03100*
- Guerra, J. A., Chuss, D. T., Dowell, C. D., et al. 2021, *ApJ*, **908**, 98
- Güsten, R., Nyman, L. Å., Schilke, P., et al. 2006, *A&A*, **454**, L13
- Hacar, A., Alves, J., Burkert, A., & Goldsmith, P. 2016, *A&A*, **591**, A104
- Hartmann, L., & Burkert, A. 2007, *ApJ*, **654**, 988
- Henney, W. J., Arthur, S. J., de Colle, F., & Mellema, G. 2009, *MNRAS*, **398**, 157
- Hoang, T., Tram, L. N., Phan, V. H. M., et al. 2022a, *AJ*, **164**, 248
- Hoang, T. D., Bich Ngoc, N., Diep, P. N., et al. 2022b, *ApJ*, **929**, 27
- Houde, M., Vaillancourt, J. E., Hildebrand, R. H., Chitsazadeh, S., & Kirby, L. 2009, *ApJ*, **706**, 1504
- Hu, Y., Lazarian, A., & Stanimirović, S. 2021, *ApJ*, **912**, 2
- Hu, Y., Lazarian, A., & Wang, Q. D. 2022, *MNRAS*, **511**, 829
- Hu, Y., Yuen, K. H., & Lazarian, A. 2018, *MNRAS*, **480**, 1333
- Hu, Y., Yuen, K. H., & Lazarian, A. 2019a, *ApJ*, **886**, 17
- Hu, Y., Yuen, K. H., Lazarian, V., et al. 2019b, *NatAs*, **3**, 776
- Indebetouw, R., Brogan, C., Chen, C. H. R., et al. 2013, *ApJ*, **774**, 73
- Indebetouw, R., de Messières, G. E., Madden, S., et al. 2009, *ApJ*, **694**, 84
- Inoue, T., & Fukui, Y. 2013, *ApJL*, **774**, L31
- Jackson, J. M., Whitaker, J. S., Rathborne, J. M., et al. 2019, *ApJ*, **870**, 5
- Kainulainen, J., Federrath, C., & Henning, T. 2014, *Sci*, **344**, 183
- Kandori, R., Tamura, M., Saito, M., et al. 2020, *ApJ*, **892**, 128
- Kennicutt, R. C. J. 1984, *ApJ*, **287**, 116
- Kim, J., Jeong, W.-S., Pak, S., Park, W.-K., & Tamura, M. 2016, *ApJS*, **222**, 2
- Kim, S., Dopita, M. A., Staveley-Smith, L., & Bessell, M. S. 1999, *AJ*, **118**, 2797
- Klein, U., Haynes, R. F., Wielebinski, R., & Meinert, D. 1993, *A&A*, **271**, 402
- Klessen, R. S. 2000, *ApJ*, **535**, 869
- Körtgen, B., Federrath, C., & Banerjee, R. 2019, *MNRAS*, **482**, 5233
- Lazarian, A. 2007, *J. Quant. Spec. Radiat. Transf.*, **106**, 225
- Lazarian, A. 2014, *SSRv*, **181**, 1
- Lazarian, A., & Pogosyan, D. 2000, *ApJ*, **537**, 720
- Lazarian, A., & Vishniac, E. T. 1999, *ApJ*, **517**, 700
- Lazarian, A., & Yuen, K. H. 2018, *ApJ*, **853**, 96
- Lazarian, A., Yuen, K. H., Ho, K. W., et al. 2018, *ApJ*, **865**, 46
- Lazarian, A., Yuen, K. H., & Pogosyan, D. 2020, *arXiv:2002.07996*
- Lazarian, A., Yuen, K. H., & Pogosyan, D. 2022, *ApJ*, **935**, 77
- Lee, M. Y., Madden, S. C., Le Petit, F., et al. 2019, *A&A*, **628**, A113
- Li, P. S., Lopez-Rodriguez, E., Ajeddig, H., et al. 2022, *MNRAS*, **510**, 6085
- Liu, J., Qiu, K., & Zhang, Q. 2022, *ApJ*, **925**, 30
- Lopez, L. A., Krumholz, M. R., Bolatto, A. D., Prochaska, J. X., & Ramirez-Ruiz, E. 2011, *ApJ*, **731**, 91
- Lu, Z., Lazarian, A., & Pogosyan, D. 2020, *MNRAS*, **496**, 2868
- Luisi, M., Anderson, L. D., Schneider, N., et al. 2021, *SciA*, **7**, eabe9511
- Mac Low, M.-M., & Klessen, R. S. 2004, *RvMP*, **76**, 125
- Mackey, J., & Lim, A. J. 2011, *MNRAS*, **412**, 2079
- Mao, S. A., McClure-Griffiths, N. M., Gaensler, B. M., et al. 2012, *ApJ*, **759**, 25
- Meixner, M., Panuzzo, P., Roman-Duval, J., et al. 2013, *AJ*, **146**, 62
- Melnick, J., Tenorio-Tagle, G., & Telles, E. 2021, *A&A*, **649**, A175
- Mestel, L. 1966, *MNRAS*, **133**, 265
- Nakajima, Y., Kandori, R., Tamura, M., et al. 2007, *PASJ*, **59**, 519
- Ngoc, N. B., Diep, P. N., Parsons, H., et al. 2021, *ApJ*, **908**, 10
- Okada, Y., Güsten, R., Requena-Torres, M. A., et al. 2019, *A&A*, **621**, A62
- Pabst, C., Higgins, R., Goicoechea, J. R., et al. 2019, *Natur*, **565**, 618
- Pabst, C. H. M., Goicoechea, J. R., Teyssier, D., et al. 2020, *A&A*, **639**, A2
- Pattle, K., Ward-Thompson, D., Hasegawa, T., et al. 2018, *ApJL*, **860**, L6
- Pellegrini, E. W., Baldwin, J. A., & Ferland, G. J. 2011, *ApJ*, **738**, 34
- Peretto, N., André, P., & Belloche, A. 2006, *A&A*, **445**, 979
- Peretto, N., Fuller, G. A., Duarte-Cabral, A., et al. 2013, *A&A*, **555**, A112
- Phillips, T. G., Huggins, P. J., Wannier, P. G., & Scoville, N. Z. 1979, *ApJ*, **231**, 720
- Pineda, J. E., Caselli, P., & Goodman, A. A. 2008, *ApJ*, **679**, 481
- Schneider, N., Röllig, M., Simon, R., et al. 2018, *A&A*, **617**, A45
- Schneider, N., Simon, R., Guevara, C., et al. 2020, *PASP*, **132**, 104301
- Santos, F. P., Chuss, D. T., Dowell, C. D., et al. 2019, *ApJ*, **882**, 113
- Schaefer, B. E. 2008, *AJ*, **135**, 112
- Schneider, N., André, P., Könyves, V., et al. 2013, *ApJL*, **766**, L17
- Schneider, N., Bontemps, S., Girichidis, P., et al. 2015, *MNRAS*, **453**, L41
- Schneider, N., Csengeri, T., Bontemps, S., et al. 2010, *A&A*, **520**, A49
- Schneider, N., Ossenkopf-Okada, V., Clarke, S., et al. 2022, *A&A*, **666**, A165
- Skalidis, R., Sternberg, J., Beattie, J. R., Pavlidou, V., & Tassis, K. 2021, *A&A*, **656**, A118
- Skalidis, R., & Tassis, K. 2021, *A&A*, **647**, A186
- Skalidis, R., Tassis, K., Panopoulou, G. V., et al. 2022, *A&A*, **665**, A77
- Soam, A., Maheswar, G., Lee, C. W., Neha, S., & Kim, K.-T. 2018a, *MNRAS*, **476**, 4782
- Soam, A., Pattle, K., Ward-Thompson, D., et al. 2018b, *ApJ*, **861**, 65
- Tahani, M., Plume, R., Brown, J. C., Soler, J. D., & Kainulainen, J. 2019, *A&A*, **632**, A68
- Tang, Y.-W., Koch, P. M., Peretto, N., et al. 2019, *ApJ*, **878**, 10
- Tiwari, M., Karim, R., Pound, M. W., et al. 2021, *ApJ*, **914**, 117
- Townsend, L. K., Broos, P. S., Feigelson, E. D., et al. 2006, *AJ*, **131**, 2140
- Tram, L. N., & Hoang, T. 2022, *FRASS*, **9**, 923927
- Tram, L. N., Hoang, T., Lopez-Rodriguez, E., et al. 2021, *ApJ*, **923**, 130
- Young, E. T., Becklin, E. E., Marcum, P. M., et al. 2012, *ApJL*, **749**, L17
- Yuen, K. H., & Lazarian, A. 2017a, *ApJL*, **837**, L24
- Yuen, K. H., & Lazarian, A. 2017b, *arXiv:1703.03026*